Life Sciences 358 (2024) 123108

Contents lists available at ScienceDirect

Life Sciences

journal homepage: www.elsevier.com/locate/lifescie

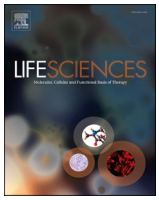

Exosomes from human bone marrow MSCs alleviate PD-1/PD-L1 inhibitor-induced myocardial injury in melanoma mice by regulating macrophage polarization and pyroptosis

Bingqian Zhou [a,1], Qin Qin [a,1], Yue Fang [a,1], Xiaoyu Liu [a], Mengyu Zhang [a], Shuo Wang [a], Li Zhong [a,b], Rui Guo [a,c,*]

[a] College of Life Sciences, Institute of Life Science and Green Development, Hebei University, Baoding 071002, China
[b] College of Osteopathic Medicine of the Pacific, Western University of Health Sciences, Pomona, CA 91766, USA
[c] The Key Laboratory of Zoological Systematics and Application, College of Life Sciences, Hebei University, Baoding 071002, China

ARTICLE INFO

Keywords:
Bone marrow mesenchymal stem cells
Exosomes
Cardiac toxicity
Immune checkpoint inhibitor
Macrophage
pyroptosis

ABSTRACT

Myocarditis, which can be triggered by immune checkpoint inhibitor (ICI) treatment, represents a critical and severe adverse effect observed in cancer therapy. Thus, elucidating the underlying mechanism and developing effective strategies to mitigate its harmful impact is of utmost importance. The objective of this study is to investigate the potential role and regulatory mechanism of exosomes derived from human bone marrow mesenchymal stem cells (hBMSC-Exos) in providing protection against myocardial injury induced by ICIs. We observed that the administration of programmed death 1/programmed death-ligand 1 (PD-1/PD-L1) inhibitor BMS-1 in tumor-bearing mice led to evident cardiac dysfunction and myocardial injury, which were closely associated with M1 macrophage polarization and cardiac pyroptosis. Remarkably, these adverse effects were significantly alleviated through tail-vein injection of hBMSC-Exos. Moreover, either BMS-1 or hBMSC-Exos alone demonstrated the ability to reduce tumor size, while the combination of hBMSC-Exos with BMS-1 treatment not only effectively improved the probability of tumor inhibition but also alleviated cardiac anomalies induced by BMS-1.

1. Introduction

Immune checkpoint inhibitors (ICIs), also known as monoclonal antibodies (mAbs), are designed to specifically target immune checkpoint molecules, and hinder the function of inhibitory receptors located on T cells. By doing so, they can activate the immune system to recognize and eliminate cancer cells through preventing the evasion of immune responses mediated by T cells [1]. In recent years, the utilization of ICIs for cancer treatment has been growing rapidly, leading to an increase in the incidence of immune-related adverse events (irAEs). According to the related reports, the occurrence rate of irAEs in patients receiving ICI treatment can be reach as high as 54 % to 76 % [2]. ICIs can cause severe and potentially fatal cardiac toxicities, such as myocarditis, pericarditis, arrhythmia, and heart failure [3,4]. Once myocardial injury occurs, it can rapidly progress and result in the highest mortality rate [5,6]. Therefore, there is an immediate need to identify effective treatments that can alleviate cardiac injuries associated with ICIs.

Over the last decade, the immunomodulatory capabilities of mesenchymal stem cells (MSCs) have provided promise for the treatment of various immune-related disorders including cardiac abnormalities. Nevertheless, there is an ongoing debate regarding the safety of MSCs, particularly with regards to their possible role in promoting tumorigenesis [7,8]. Besides, the replacement of damaged tissue is almost incapable in adult mammalian heart due to the low proliferation rate of adult cardiomyocytes, which seriously hinders the myocardial regeneration [9]. Although stem cell therapy has emerged as a promising avenue for repairing and regenerating cardiac tissue, the direct transplantation of stem cells into the body or heart carries potential risks such as immune responses and cardiac electrical abnormalities. In contrast, MSC-secreted exosome (MSC-Exo) is a type of small extracellular vesicle (EV) with an average diameter of 100 nm, secreted by endosomes [10]. Exosomes which contain multiple bioactive substances

* Corresponding author at: College of Life Sciences, Institute of Life Science and Green Development, Hebei University, Baoding 071002, China.
E-mail address: rguo@hbu.edu.cn (R. Guo).
[1] These authors contributed equally to this article.

https://doi.org/10.1016/j.lfs.2024.123108
Received 29 May 2024; Received in revised form 30 September 2024; Accepted 1 October 2024
Available online 5 October 2024

have been shown to possess similar reparative properties as MSCs, while also exhibit significant anti-inflammatory and anti-cancer properties [11]. Therefore, MSC-Exos are considered to be an important way for MSCs to perform physiological functions. In animal models, MSC-Exos have demonstrated remarkable therapeutic effects on myocardial infarction and cardiac ischemic-reperfusion-induced injury [12–15].

Pyroptosis and associated inflammatory responses are common factors in various heart-related diseases, such as myocardial infarction [16], heart failure [17], diabetic cardiomyopathy [18], and viral myocarditis [19]. These pathological processes can result in cell swelling, formation of bubble-like protrusions, rupture of the plasma membrane, and secretion of pro-inflammatory cytokines [20]. MSC-derived vesicles were found to exhibit comparable biological properties to MSCs, including low immunogenicity, immunomodulatory capabilities, and the ability to home in on inflammatory or injured sites [21–23]. Moreover, Zeng et al. found that exosomes derived from bone marrow mesenchymal stem cells (BMSC-Exos) attenuated NLRP3 inflammasome-mediated pyroptosis by promoting AMPK-dependent autophagy flux [24]. Liu et al. found that BMSC-Exos could inhibit NLRP3 inflammasome-mediated inflammation and pyroptosis by modulating microglial polarization, thereby improving brain I/R damage [25]. Therefore, these characteristics allow MSC-Exos to exert a potential role in ICI-induced myocarditis and cardiac dysfunction.

Macrophages are important in regulating inflammation which is often associated with pyroptosis [26–28]. Various studies have emphasized the significance of macrophages in heart disease models [29–31]. Currently, there is increasing evidence that ICIs cause cardiac damage and are associated with macrophage polarization [32,33]. Chen et al. observed that PD-1/PD-L1 inhibitors induced M1 polarization of colonic macrophage, systemic inflammatory response and cardiac injury [34]. Similarly, the administration of PD-1 antibodies in mice resulted in the polarization of cardiac macrophages towards the M1 phenotype, which was accompanied by the upregulation of miR-34a in myocardial cells, and ultimately leading to cardiac injury [35]. These findings highlight the significance of modulating macrophage polarization as a critical approach for treating and alleviating cardiac injury induced by ICIs.

Evidence suggests that MSC-Exos have the ability to trigger macrophage conversion to anti-inflammatory M2 phenotype in the models of myocardial infarction [36] and myocardial ischemia-reperfusion [37]. Xu et al. found that the AKT1/AKT2 signaling may be involved in the regulation of macrophage polarization to reduce apoptosis and infiltration of cardiomyocytes following the administration of MSC-Exos [38]. However, little is known about the role of MSC-Exos in ICI-induced cardiac side effect. Additionally, the potential anti-cancer effect of MSC-Exos has yet to be entirely explored. To this end, this study aims to investigate the potential mechanism and role of exosomes secreted by human bone marrow mesenchymal stem cells (hBMSC-Exos) in mitigating myocarditis and myocardial injury caused by PD-1/PD-L1 binding inhibitor during the treatment of tumors. We also evaluate the contribution of hBMSC-Exos to the anti-cancer effect.

2. Materials and methods

2.1. Single-cell RNA sequencing data analysis for human samples

We downloaded the dataset GSE180045 containing 10× scRNA-seq data with three samples of control patients and two samples of patients diagnosed with myocarditis [39]. We processed single-cell sequencing data by the following methods. We utilized the "Seurat" R package to transform 10× scRNA-seq data into Seurat objects, filtering out low-quality cells based on gene count and mitochondrial gene percentage. The top 2000 highly variable genes were identified using the "FindVariableFeatures" program, and included for PCA and UMAP analysis to identify cell subpopulations. Cell type markers were obtained from the CellMarker website and previous studies. "FindMarkers" package was used to find DEGs in macrophage or monocyte cells between myocarditis and control group.

2.2. RNA-sequencing data analysis

We used the key word "pyroptosis" to search the datasets in the GeneCards (https://www.genecards.org/) and got the common genes between the human DEGs and pyroptosis genes. We constructed a PPI network with these genes as well as IL-18, PYCARD, and NLRP3. The results of the PPI analysis were imported into the Cytoscape software. The adjust p-value < 0.05 was regarded as statistically different for a filtering condition. We also used the keywords "myocarditis" to search the myocarditis datasets in the Gene Expression Omnibus (GEO) database. The retrieved results were then filtered by the species of *Mus musculus*. Finally, we selected GSE225099 dataset that defined as the training set, containing three mice with myocarditis and four healthy control mice [40]. Differential expression analysis was performed by using R software (version 4.3.0). We set a threshold at $|\log FC| \geq 1$ to screen out DEGs. The adjusted $p < 0.05$ was regarded. We used the key word "pyroptosis" to search the datasets in the Mouse Genome Informatics (https://www.informatics.jax.org/) and got the common genes between the mice DEGs and pyroptosis genes.

2.3. Gene set enrichment analysis (GSEA)

GSEA was conducted to investigate the biological processes and signaling pathways linked with these genes. The analysis involved calculating the correlation between the key genes and all other genes in the entire dataset, and then ranking the gene sets based on this correlation. Using the GO and KEGG data files as a reference, the enrichment of biological processes and signaling pathways for each gene set was assessed to identify significantly enriched functions and pathways. GSEA was performed by using R software (version 4.3.0). We set a threshold at $|NES| \geq 1$ and adjusted p-value < 0.05 being the screening criteria to identify the significant pathways.

2.4. Animals and experimental design

This study was conducted following approval from the Ethics Committee of Hebei University and the Experimental Animal Management and Use Committee. Male C57BL/6 N mice (6 weeks old) were purchased from Beijing Vital River Laboratory Animal Technology Co., Ltd. (Beijing, China) and were housed in a temperature-controlled facility at 23 °C with *ad libitum* access to water, under a 12-hour light/12-hour dark cycle. The relative humidity was maintained at 50 %. The mice underwent a two-week acclimatization period to adapt to the new environment prior to the initiation of the experiment, and were randomly grouped (9 mice per group). According to the previous protocol [41], B16F10 cells (2×10^5, Procell Life Science & Technology Co., Ltd., Wuhan, China) were injected to the right flank of the C57BL/6 N mice (6–7 weeks old) to establish the melanoma model. Once the tumors reached a size of approximately 50 mm^3, the mice were intraperitoneally injected with BMS-1 (10 mg/kg/time) for a total of 6 injections every other day, with or without hBMSC-Exos treatment (1 μg/μL, 8 mg/kg) [33]. hBMSC-Exos were administered *via* the caudal vein of the mice every 7 days, with a total of 2 injections. Another batch of mice (6 mice per group) was treated in the same manner to evaluate the effect of both BMS-1 and hBMSC-Exos on tumor growth. The body weights of mice were measured every two days throughout the entire experimental period. On the last day of the treatment, the hearts, livers, spleens, and kidneys of the mice were weighed. When the average tumor size of mice reached 2000 mm^3, the animals were euthanized timely in accordance with the *AVMA Guidelines for the Euthanasia of Animals: 2020 Edition*. In order to evaluate the effect of PD-1 antibody, anti-PD-1 monoclonal antibody (Thermo Fisher Scientific, 14-9982-82) at 200 μg per mouse were injected to the mice through tail vein injection [42], followed by cardiac function assessment by echocardiographic evaluation,

myocardial injury detection by ELISA assay and inflammatory detection by qRT-PCR.

2.5. Echocardiographic evaluation

An Echocardiographic assessment was performed on the last day of the experimental period. Mice were anesthesia using 1.2 % isoflurane administered with a calibrated vaporizer and an inhalant (Sigma Delta, Penlon, Oxford, UK). The cardiac geometry and function of mice were then determined with a two dimensional (2D) guided M-mode echocardiography (VINNO 6 LAB, VINNO, Beijing, China) which equipped with a 23 MHz linear transducer. The echocardiographic images of the hearts were captured in the 2D-mode in the parasternal long-axis view with a depth of 2 cm. The M-mode cursor was positioned perpendicular to the interventricular septum and posterior wall of the left-ventricle (LV) at the level of papillary muscles from the 2D-mode. End-diastolic septal thickness (IVSd), end-systolic septal thickness (IVSs), left ventricular diastolic and systolic posterior wall thickness (LVPWd, LVPWs), ejection fraction (EF), fractional shortening (FS), the LV end-diastolic diameter (LVEDD), LV end-systolic diameter (LVESD), LV mass, stroke volume (SV), cardiac output (CO), end-diastolic left ventricular anterior wall thickness (LVAWd), end-systolic left ventricular anterior wall thickness (LVAWs), end diastolic left ventricular volume (LV Volume d) and end systolic left ventricular volume (LV Volume s) were measured. Wall thickness was calculated as the average of LVPWd and LVPWs. The data were presented as the mean values of these parameters (mean ± SEM).

2.6. Immunohistochemical and histological analysis

After anesthesia, the mice were euthanized. The hearts were excised and immediately placed in 10 % neutral formalin, which was kept at room temperature for 24 h. The specific technical procedures after fixing the cardiac tissue were carried out by Servicebio, Inc. (Wuhan Servicebio Technology Co., Ltd., Wuhan, Hubei, China) according to their standard operating procedures. Briefly, the fixed tissue was dehydrated using a series of alcohol concentration gradients and cleared using xylene. The tissue was then infiltrated with liquid paraffin and embedded in paraffin blocks. The specimens were cut into 5 μm sections. For hematoxylin and eosin (HE) staining, slides were dewaxed and then stained with hematoxylin and eosin. For Immunohistochemical staining, the slides performed the deparaffinization and antigen retrieval [43]. Subsequently, the sections were treated with 0.03 % H_2O_2 for 25 min, pre-incubated with rabbit serum and labelled with rabbit anti-mouse primary polyclonal antibodies targeting iNOS (1:500, GB111119, Servicebio) and CD163 (1:500, GB113751, Servicebio) which are the surface markers of M1 and M2 macrophages [44]. The slices were sequentially incubated with the HRP-linked goat anti-rabbit IgG (1:200, GB23303, Servicebio) and 3,3′-diaminobenzidine (DAB, G1212, Servicebio). Afterward, they were washed with tap water and stained with hematoxylin (G1004, Servicebio). Images of three randomly selected fields were captured at 400× magnification under an optical microscope (Olympus CKX53, Olympus, Tokyo, Japan). The Integrated option density (IOD) and the area of the positive regions within the images were analyzed using Image J software (Fiji, National Institutes of Health, Bethesda, MD, USA). The average optical density (AOD) was calculated using the following formula: AOD = IOD / Area, and the data were presented as the mean of AOD (mean ± SEM).

2.7. Isolation and culture of mouse peritoneal macrophages

The isolation and culture of peritoneal macrophages were conducted according to previously described protocols [45]. Mice were sacrificed by quick and humane cervical dislocation [46]. 5 mL of RPMI 1640 medium (Thermo Fisher Scientific, Gaithersburg, MD, USA) supplemented with 100 U/mL penicillin and streptomycin (Biodragon, Beijing, China) was injected into the abdomen using a syringe for peritoneal lavage. Lavage fluid was then withdrawn from the peritoneal cavity of the mice with a syringe and centrifuged at 4 °C, 1000 rpm for 5 min. The supernatant was discarded and the cells were resuspended in complete medium (RPMI 1640 medium supplemented with 10 % (v/v) bovine calf serum (ExCell Bio, Shanghai, China), 100 U/mL penicillin and 100 U/mL streptomycin) and then allowed to attach in the 12-well plate for 2 h at 37 °C in a humidified incubator containing 5 % CO_2. After washing away the floating cells with PBS, fresh medium was added. The phagocytic activity of mouse peritoneal macrophages was evaluated by an ink phagocytosis test. Following the addition of 10 μL of India ink (PHYGENE, Fuzhou, Fujian, China) and an incubation period at 37 °C for 4 h, the mouse peritoneal macrophages were captured in images using an inverted phase contrast microscope (Olympus CKX53, Olympus, Japan).

2.8. Cell culture and treatment

Mouse melanoma B16F10 cells and RAW264.7 cells were obtained from Procell Life Science & Technology Co., Ltd. (Wuhan, China). HL-1 cells were purchased from BeNa Culture Collection (Beijing, China). Human bone marrow mesenchymal stem cells (hBMSCs) were obtained from Qing Qi Biotechnology Development Co., Ltd. (Shanghai, China). B16F10 cells were cultured in RPMI 1640 medium (Thermo Fisher Scientific, Gaithersburg, MD, USA) supplemented with 10 % fetal bovine serum (ExCell Bio, Uruguay) and 100 U/mL penicillin-streptomycin (Biodragon, Beijing, China). HL-1, RAW264.7 and hBMSCs were cultured in Dulbecco's modified Eagle's medium (DMEM) (Thermo Fisher Scientific, Gaithersburg, MD, USA) supplemented with 10 % fetal bovine serum (ExCell Bio, Uruguay) and 100 U/mL penicillin-streptomycin. All cells were maintained in a humidified atmosphere containing 5 % CO_2 at 37 °C. To investigate the potential direct effect of PD-1/PD-L1 inhibitor on cardiac muscle cell damage and inflammation, HL-1 cardiomyocytes were treated with BMS-1 at concentrations of 1 μg/mL and 5 μg/mL for a duration of 24 h [47]. Additionally, RAW264.7 cells were exposed to LPS (1 μg/mL) for 24 h to assess its influence on macrophage polarization. Furthermore, HL-1 cells were co-cultured with RAW264.7 cells in the presence or absence of LPS (1 μg/mL) for 24 h, followed by treatment with hBM-Exos (40 μg/mL) for 4 h, aiming to investigate the impact of macrophage polarization on pyroptosis in cardiomyocytes.

2.9. Immunofluorescence staining and imaging

RAW264.7 cells and HL-1 cells were cultured on glass slides and subjected to immunofluorescence staining as described previously [48,49]. In brief, the specimens were blocked with 10 % goat serum, followed by overnight incubation with rabbit anti-mouse primary monoclonal antibodies against TNF-α (1:500, Proteintech, 60291-1-Ig), Arg-1 (1:500, Proteintech, 16001-1-AP), and ASC (1:500, Bioss, bs-6741R) at 4 °C. They were then incubated with secondary antibodies, including Dylight 488-conjugated goat anti-rabbit IgG (1:500; Abbkine, A23220), Dylight 488-conjugated goat anti-mouse IgG (1:500; Abbkine, A23210), or Cy3-conjugated goat anti-rabbit IgG (1:500; ABclonal, AS007) for 1 h at room temperature. Finally, the slides were counterstained with 4,6-diamino-2-phenyl indole (DAPI) (MCE, NJ, USA) and imaged using a laser scanning confocal microscope (Olympus LSM900, Olympus, Tokyo, Japan).

2.10. RNA isolation and qRT-PCR analysis

The RNAs were extracted from mouse heart, RAW264.7, and HL-1 cells by using the RNAiso Plus kit (Tiangen Biotech, Beijing, China) following the manufacturer's instructions. The extracted RNAs were reverse transcribed into cDNAs using the FastKing cDNA first strand Synthesis Kit (Tiangen Biotech, Beijing, China) in accordance with the

manufacturer's protocol. Briefly, a total reaction volume of 10 μL was prepared by mixing 0.25 μg of RNA, 2 μL of 5× reaction mix, and RNase-free water. The mixture was incubated and reacted in a thermal cycler at 25 °C for 5 min, 46 °C for 20 min, and finally at 95 °C for 1 min. Primers were designed using NCBI BLAST and were listed in Table S1. The qRT-PCR was performed on a CFX96 Touch Real-Time PCR Detection System using SYBR Green. A total reaction volume of 10 μL, containing forward and reverse primers (10 μM), cDNA, and DEPC water were prepared and mixed. The sample was subjected to an initial denaturation step at 95 °C for 2 min, followed by a specific thermal cycling program (5 s at 95 °C, 30 s at 60 °C, 30 s at 72 °C) for a total of 40 cycles. The obtained results were normalized to the expression of mouse 18S. Each group processed three independent experiments, and each sample was tested in triplicate.

2.11. Exosome extraction and purification

Exosomes derived from hBMSCs were isolated from the medium *via* ultracentrifugation following the method described by Liu et al. [50]. Once cells were reaching 80 % confluency, the cell culture supernatant was replaced with serum-free medium. After being cultured for 48 h, the medium was collected into sterile tubes and underwent centrifugation at 300*g*, 2000*g*, and 7000*g* for 10 min, 20 min, and 1 h, respectively, in order to eliminate cellular debris and other larger extracellular vesicles. The harvested supernatant was then filtered through a 100 KD ultrafiltration centrifuge tube (BIOFIL, Fuzhou, Fujian, China) at 5000*g* for 5 min to expel the unwanted vesicles. Subsequently, the filtered supernatant was ultra-centrifugated using Ultra-Clear™ tubes (Beckman Coulter, Brea, CA, USA) and Optima MAX-TL (Beckman Coulter, Brea, CA, USA) at 150,000*g* for 2 h. The collected exosomes were then resuspended in PBS and finally stored at −80 °C. The protein concentration of the isolated exosomes was measured using a BCA protein assay kit (Solarbio Life Science, Beijing, China).

2.12. Exosome characterization

The shape and ultrastructure of the extracted exosomes were observed using transmission electron microscopy (TEM, JEM-100SX, JEOL, Tokyo, Japan). The exosomes were counterstained with uranyl acetate for 2–3 min for observation. After diluting the original exosome samples by 2000 times, we determined their nanoparticle size distribution and concentration by using a Nanoparticle Tracking Analysis device (NTA, ZetaView PMX 110, Particle Metrix, Germany). The distribution curves and particle concentration were automatically generated. Additionally, the exosome markers including CD63, TSG101 and Alix, as well as GAPDH were verified through Western blotting.

2.13. Exosome uptake assay

The hBMSC-Exos were labelled with red fluorescent using the PKH26 Red Fluorescent Exosome Labeling Kit (Umibio, Shanghai, China) as per the manufacturer's instructions. Specifically, the PKH26 linker was diluted to 100 μM and mixed with the exosome suspension at a ratio of 0.5 μL/μg. Following a 10-minute incubation at room temperature, the fluorescently labelled hBMSC-Exos were separated by ultracentrifugation at 100,000*g* for 2 h. The precipitate was then resuspended in PBS, and protein quantification was performed using a BCA assay kit (Solarbio Life Science, Beijing, China). The RAW264.7 cells were cultured on glass slides in the presence of 50 μg/mL of fluorescently labelled hBMSC-Exos. After 24 h of incubation and staining with 4,6-diamino-2-phenylindole (DAPI) (MCE, NJ, USA), cells were observed using a laser scanning confocal microscope (Olympus LSM900, Olympus, Tokyo, Japan).

2.14. Protein extraction and western blot analysis

Cardiac tissue was harvested and total proteins were extracted using premixed radioimmunoprecipitation assay (RIPA, Solarbio, Beijing, China) and phenylmethyl sulfonyl fluoride (PMSF) (CW-BIO, Beijing, China) at a low temperature on ice. Protein quantification was determined using a bicinchoninic acid (BCA) protein quantification kit (Solarbio, Beijing, China) and a microplate reader (Molecular Devices, Silicon Valley, CA, USA). Equal amounts of proteins (20–50 μg protein/lane) obtained from hBMSC-Exos or extracted from cardiac tissue were mixed with 5× loading buffer and boiled at 100 °C for 10 min. A 12 % sodium dodecyl sulfate-polyacrylamide gel (SDS-PAGE) was utilized to separate the proteins, which were then electrophoretically transferred to polyvinylidene fluoride (PVDF) membranes (0.2 μm pore size, Merck-Millipore, Billerica, MA, USA). The membranes were blocked with 5 % (w/v) skim milk and incubated with ALIX (1:1000, ab186728, Abcam), CD63 (1:1000, ab1344045, Abcam), TSG101 (1:1000, ab133586, Abcam), Caspase-1 P20 (1:1000, bs-10442R, Bioss), ASC (1:1000, bs-6741R, Bioss), GSDMD (1:2000, 20770-1-AP, Proteintech), NLRP3 (1:1000, 19771-1-AP, Proteintech), Cleaved-GSDMD (1:1000, 101375, Cell Signaling Technology), β-actin (1:2000, 66009-1-lg, Proteintech) and GAPDH (1,1000, PTM-5375, PTMBio) antibodies. After washing, the blots were incubated with horseradish peroxidase (HRP)-linked anti-rabbit IgG (1,5000; Cell signaling technology, 7074P2). An electrochemiluminescence (ECL) western blotting substrate (Solarbio Life Science, Beijing, China) was used to visualize the membrane. The gel images were captured by using a Bio-Rad ChemiDoc XRS+ system (Bio-Rad, Hercules, CA, USA) and the results were analyzed by image lab software.

2.15. ELISA

The cTnI, CK-MB and IL-18 concentrations in mouse serum were measured by cTnI ELISA kit (JINGMEI BIOTECHNOLOGY, Shanghai, China), CK-MB ELISA kit (JINGMEI BIOTECHNOLOGY, Shanghai, China) and IL-18 ELISA kit (Beyotime, Shanghai, China) according to the instructions provided by the manufacturer.

2.16. Flow cytometry

Cells collected from peritoneal lavage were divided into two groups, one of which was labelled with FITC anti-mouse F4/80 (123107, BioLegend, San Diego, USA), while the other was labelled with FITC anti-mouse IgG (406001, BioLegend, San Diego, USA). RAW264.7 cells subjected to different treatments were labelled with FITC anti-mouse F4/80 (123107, BioLegend, San Diego, USA), APC anti-mouse CD86 (105012, BioLegend, San Diego, USA), and APC anti-mouse CD206 (141707, BioLegend, San Diego, USA), respectively. The labelled cells underwent flow cytometry analysis (CytoFLEX S, Beckman Coulter, California, USA). The F4/80-positive cells extracted from peritoneal lavage were identified as macrophages. RAW264.7 cells expressing both F4/80 and CD86 were classified as M1 macrophages, whereas cells expressing both F4/80 and CD206 were classified as M2 macrophages. Data were analyzed through CytExpert software Version 2.4 (CytExpert, Beckman Coulter, California, USA).

2.17. Statistical analysis

All data were shown as mean ± standard error of the mean (SEM). Statistical analysis was performed using GraphPad Prism software (GraphPad Software, San Diego, CA, USA). Comparisons between multiple groups were assessed by one-way ANOVA with the Tukey test. Comparisons between two groups were assessed by unpaired *t*-test. $p < 0.05$ was considered significant.

3. Results

3.1. Single-cell transcriptomics analysis in human samples

A cluster of macrophage or monocyte cells were identified based on the expression of markers for macrophages and monocytes including CD68, CD14 and CD163 (Fig. 1A–D) in human GSE180045 dataset. There were 802 differentially expressed genes (DEGs) (286 up-regulated and 516 down-regulated) by comparing the macrophage or monocyte cells in the myocarditis group to the control group. The DEGs were displayed in the volcano plot (Fig. 1E). Among which, we got 37 DEGs (12 up-regulated and 25 down-regulated) related to pyroptosis (Table S2). We constructed a protein-protein interaction (PPI) network that includes the overlapping genes along with IL-18, PYCARD, and NLRP3. The results of the PPI analysis were then imported into the Cytoscape software, and the PPI network revealed significant

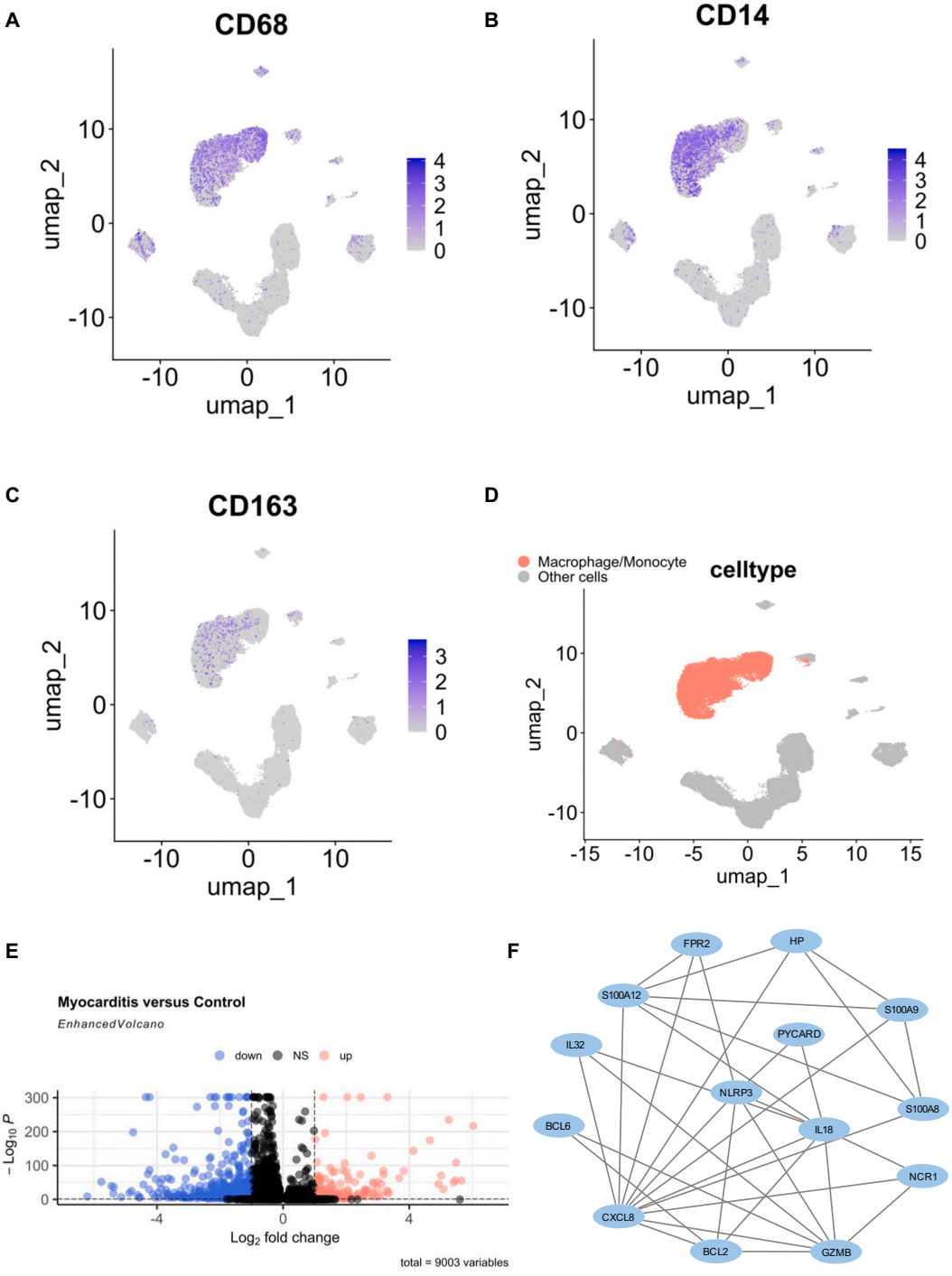

Fig. 1. Identification and analysis of macrophages in blood of patients.
(A–C) Feature plots of key immune canonical markers in the clusters. **(D)** Detection of cell clusters consisting of macrophages and monocytes in all samples. **(E)** Volcano plot of DEGs displays a total of 802 DEGs (286 up-regulated and 516 down-regulated) in GSE180045. Differential gene expression analysis using the log2 Fold Change and p value. The red dots represent genes that are upregulated with a threshold at $|\log FC| \geq 1$ and p-value < 0.05, while the blue dots represent genes that are downregulated. **(F)** PPI network of DEGs in datasets GSE180045.

interactions among these genes (Fig. 1F).

3.2. Differential expressions of pyroptosis genes in myocarditis mice

We screened a total of 2542 DEGs (1826 up-regulated and 716 down-regulated) in GSE225099. The results of RNA-seq expression matrix were displayed in the volcano plots (Fig. 2A). Therein, 19 DEGs related to pyroptosis were screened out and visualized in the form of a heatmap (Fig. 2B). All genes related to pyroptosis are upregulated. In addition, the Gene Set Enrichment Analysis (GSEA) for possible related signaling pathways of total DEGs indicated that the interferon gamma response, inflammatory response and oxidative phosphorylation were significantly enriched in biological processes (Fig. 2C). Among which, *Zbp1* exhibited the highest fold increase. *Zbp1* gene expression level was nearly 16-fold upregulated in myocarditis compared to control heart. These results demonstrated the presence of pyroptosis in mice with myocarditis induced by ICIs. The DEGs related to pyroptosis and the results of GSEA were summarized in the supplementary excel 1 and 2.

3.3. Effect of PD-1 antibody on cardiac function in melanoma mice

Following the treatment with PD-1 antibody, echocardiograms of melanoma-bearing mice revealed a significant compromise in left ventricular contractile function compared to the control group (Fig. S1A–D). As depicted in Fig. S1C–D, treatment with PD-1 antibody notably decreased the percentages of ejection fraction (EF%) and fractional shortening (FS%) ($p < 0.01$). We also observed that the concentration of cTnI and CK-MB in the mouse serum was significantly higher after PD-1 antibody administration (Fig. S1E–F). Additionally, further qRT-PCR analysis showed a significant upregulation in the expression of iNOS ($p < 0.05$), TNF-α ($p < 0.001$), and IL-6 ($p < 0.001$) in heart tissue following PD-1 antibody treatment (Fig. S1G–I). These findings indicated that the use of PD-1 antibody resulted in cardiac dysfunction associated with inflammation.

3.4. Direct effect of PD-1/PD-L1 inhibitor on myocardial damage and macrophage polarization

To explore the potential direct effect of the PD-1/PD-L1 inhibitor BMS-1 on myocardial inflammatory injury, HL-1 cardiomyocytes were treated with different concentrations of BMS-1 (1 μg/mL and 5 μg/mL). The expression levels of inflammatory factors such as *Tnf-α, Il-6, Il-1β* (Fig. 3A–C), as well as pyroptotic markers including *Nlrp3, Pycard* and *Il-18* (Fig. 3D–F) were assessed. As depicted in Fig. 3A–F, no significant alterations in the expression of these markers were observed in cells treated with BMS-1 compared to the control group. Furthermore, Fig. 3G demonstrated that HL-1 cardiomyocytes maintained their normal cellular state regardless of the presence of BMS-1, indicating that the PD-1/PD-L1 inhibitor did not directly induce severe pyroptotic damage and cellular phenotype in cardiomyocytes. To assess the impact of PD-1/PD-L1 inhibitor on the polarization of mouse macrophages, primary peritoneal macrophages were extracted from mice *via* peritoneal lavage. Microscopic examination (Fig. 3H) and ink phagocytosis experiment (Fig. 3I) revealed that the extracted macrophages exhibited good morphology and robust phagocytosis ability. Following treatment with BMS-1 at concentrations of 1 μg/mL and 5 μg/mL, there was a significant increase in the expression of M1 macrophage markers (Fig. 3J) in the primary mouse peritoneal macrophages compared to the control. Flow cytometry analysis showed that there were 82.79 % cells extracted from peritoneal lavage expressed the F4/80 marker (Fig. 3K–L). These results indicated that PD-1/PD-L1 inhibitor can directly induce M1-type polarization of primary mouse peritoneal macrophages.

3.5. Identification and cellular internalization of hBMSC-Exos

Exosomes were initially extracted and purified from the medium of bone marrow mesenchymal stem cells (hBMSCs) using a combination of differential centrifugation and ultra-high-speed centrifugation (Fig. 4A). The subsequent morphological assessment using transmission electron microscopy (TEM) showed that the exosomes exhibited characteristic round-like structures with "cup-shaped" morphology (Fig. 4B). The results of the nanoparticle tracking analysis (NTA) revealed that the majority of hBMSC-Exos had diameters ranging from 100 to 150 nm. Following a dilution of 2000 times, the extracted exosome samples exhibited an average concentration of 7.9×10^7 particles/mL. The original concentration of the hBMSC-Exos is about 1.6×10^{11} particles/mL (Fig. 4C). Positive results were obtained from Western blot analysis of exosome markers including TSG101, ALIX, and CD63 proteins (Fig. 4D), suggesting hBMSC-Exos were successfully extracted from BMSCs. As shown in Fig. 2E, hBMSC-Exos were able to penetrate the cell membrane of the macrophage, and become internalized within the cytoplasm.

3.6. hBMSC-Exos ameliorated PD-1/PD-L1 inhibitor-induced cardiac anomalies in melanoma mice

To investigate the effect of hBMSC-Exos on myocardial injury induced by PD-1/PD-L1 inhibitor during the treatment of tumors, we established a melanoma mouse model followed by the BMS-1 treatment with or without tail-vein injection of hBMSC-Exos. The representative echocardiographic images were shown in Fig. 5A. The results obtained from Fig. 5B–C and Table S3 revealed that the administration of BMS-1 led to a significant reduction in the ejection fraction (EF), fractional shortening (FS), LVPWs, wall thickness, and cardiac output (CO), as well as a notable increase in the end systolic left ventricular diameter (LVESD) and end systolic left ventricular volume (LV volume s). Intriguingly, these adverse alterations were alleviated by hBMSC-Exos. The treatment with hBMSC-Exos alone showed normal cardiac function, there were no alterations in these parameters when compared to the control group. Furthermore, the results in Fig. 5D and Table S4 displayed that the BMS-1 markedly increased the heart weight when normalized to the body weight. However, this effect was significantly reversed by the administration of hBMSC-Exos. Neither BMS-1 nor hBMSC-Exos had any significant impact on liver and spleen weights, although BMS-1 administration resulted in a notable increase in kidney weight when normalized to body weight (Fig. 5E–G). In addition, prolonged BMS-1 administration led to a significant reduction in the body weight of mice. This adverse effect was mitigated by the hBMSC-Exos treatment (Fig. 5H). These results suggested that PD-1/PD-L1 inhibitor treatment in melanoma mice caused a decline in cardiac systolic function, which was significantly improved by the application of hBMSC-Exos. HE staining revealed abnormalities of the cardiomyocyte of BMS-1 treated mice compared to the control group. We observed cardiomyocyte necrosis (indicated by black arrows), nuclear condensation, myofibrillar rupture, cytoplasmic vacuolization and myocytolysis in peripheral cardiomyocytes (indicated by green arrows), and occasional lymphocyte infiltration (indicated by blue arrows) in BMS-1-treated mice (Fig. S2A–B). Interestingly, after the treatment with hBMSC-Exos, there was no obvious necrosis or inflammatory cell infiltration, except for a few cardiomyocytes exhibiting myocytolysis (green arrows, Fig. S2C). There was no significant difference between hBMSC-Exos alone group and the control group (Fig. S2D).

3.7. hBMSC-Exos suppressed LPS-induced M2 to M1 polarization of RAW 264.7 macrophages

To investigate the mechanism underlying the protective effect of hBMSC-Exos against PD-1/PD-L1 inhibitor-induced myocardial injury, we induced M1 polarization of RAW 264.7 macrophage cell lines directly by using LPS. Under microscopic examination, pseudopodia were observed to be differentiated from RAW 264.7 cells following LPS treatment (Fig. 6A). The immunofluorescence image revealed a

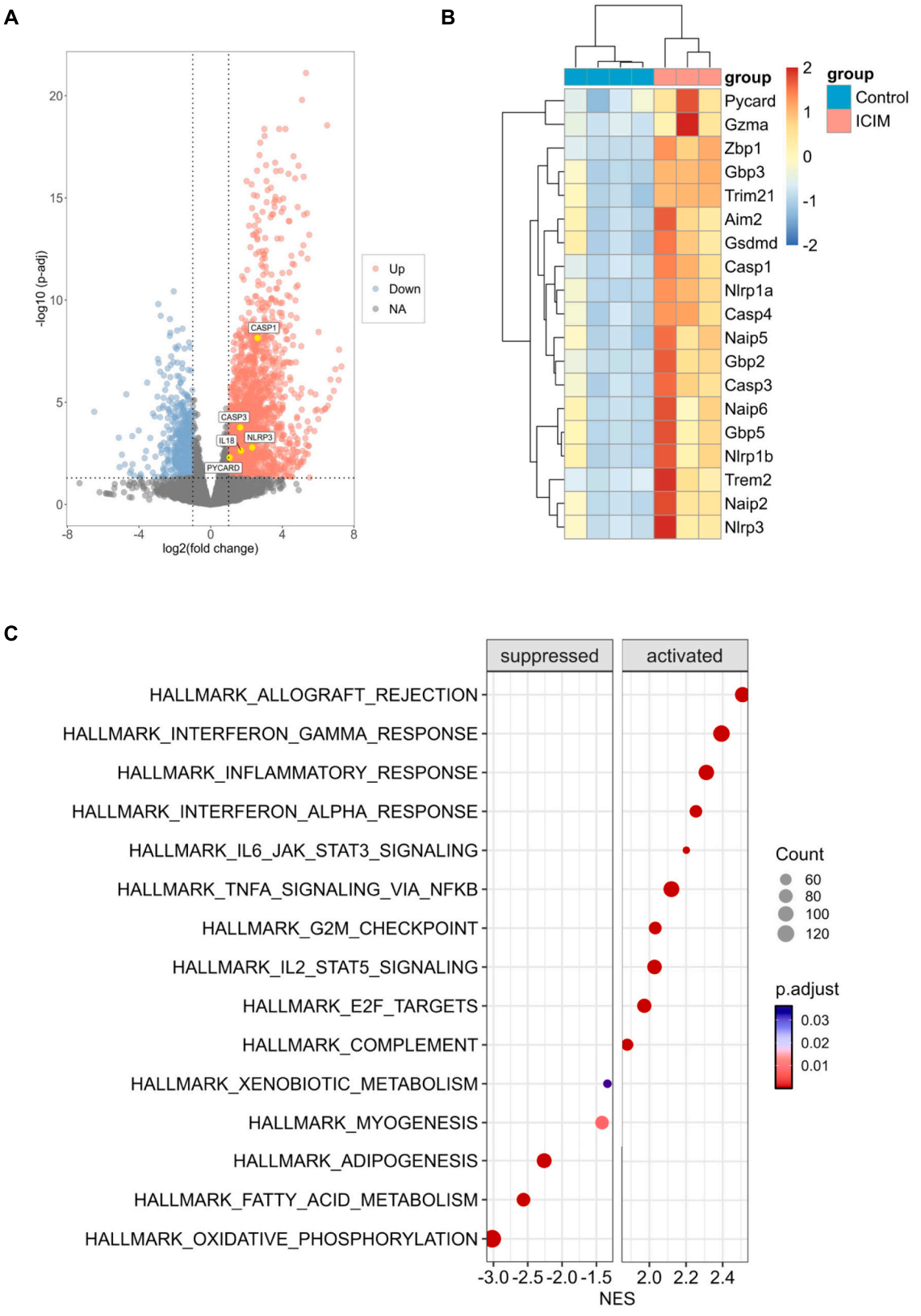

Fig. 2. Identification and enrichment of DEGs in mice.
(A) Volcano plot of DEGs displays a total of 2542 DEGs (1826 up-regulated and 716 down-regulated) in GSE225099. **(B)** The heatmap displays the 19 DEGs identified from GSE22509 dataset related to pyroptosis. Red and blue represent upregulated and downregulated gene expression, respectively. ICIM: Immune checkpoint inhibitor-induced myocarditis. **(C)** GSEA plot for pathways significantly enriched in GSE225099. NES: normalized enrichment score.

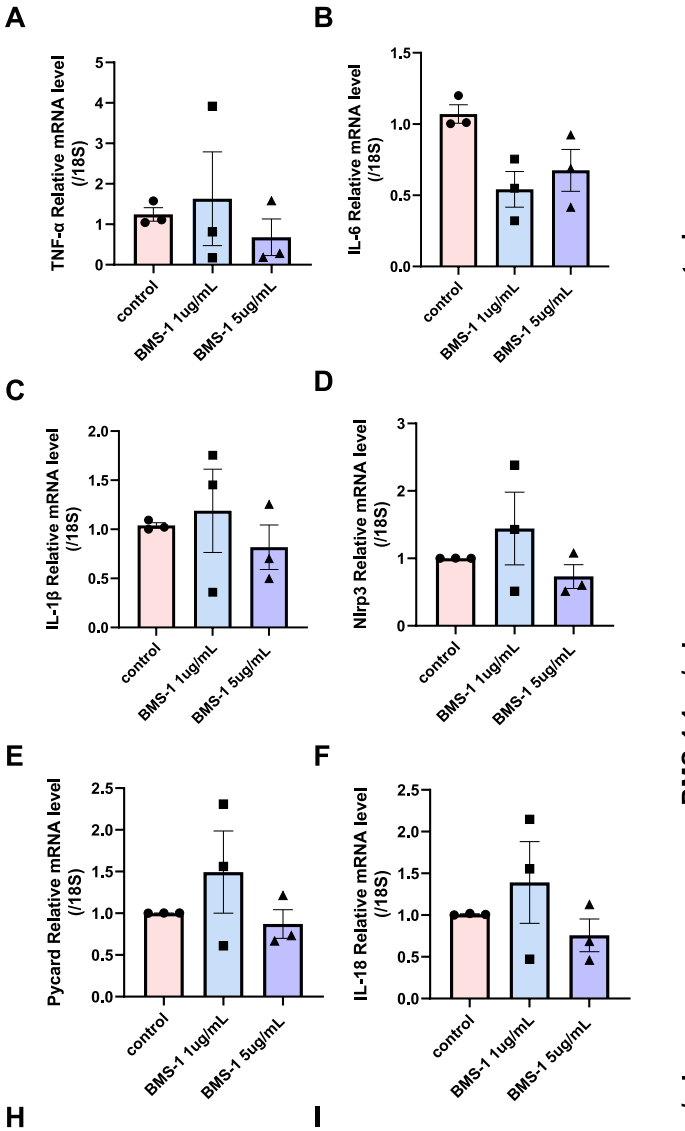

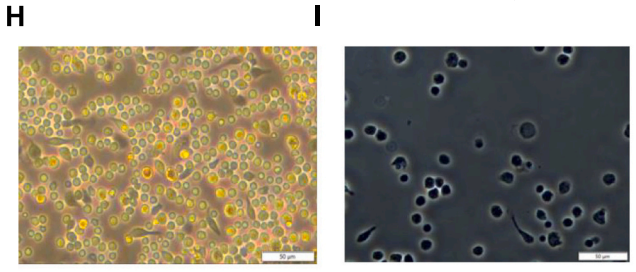

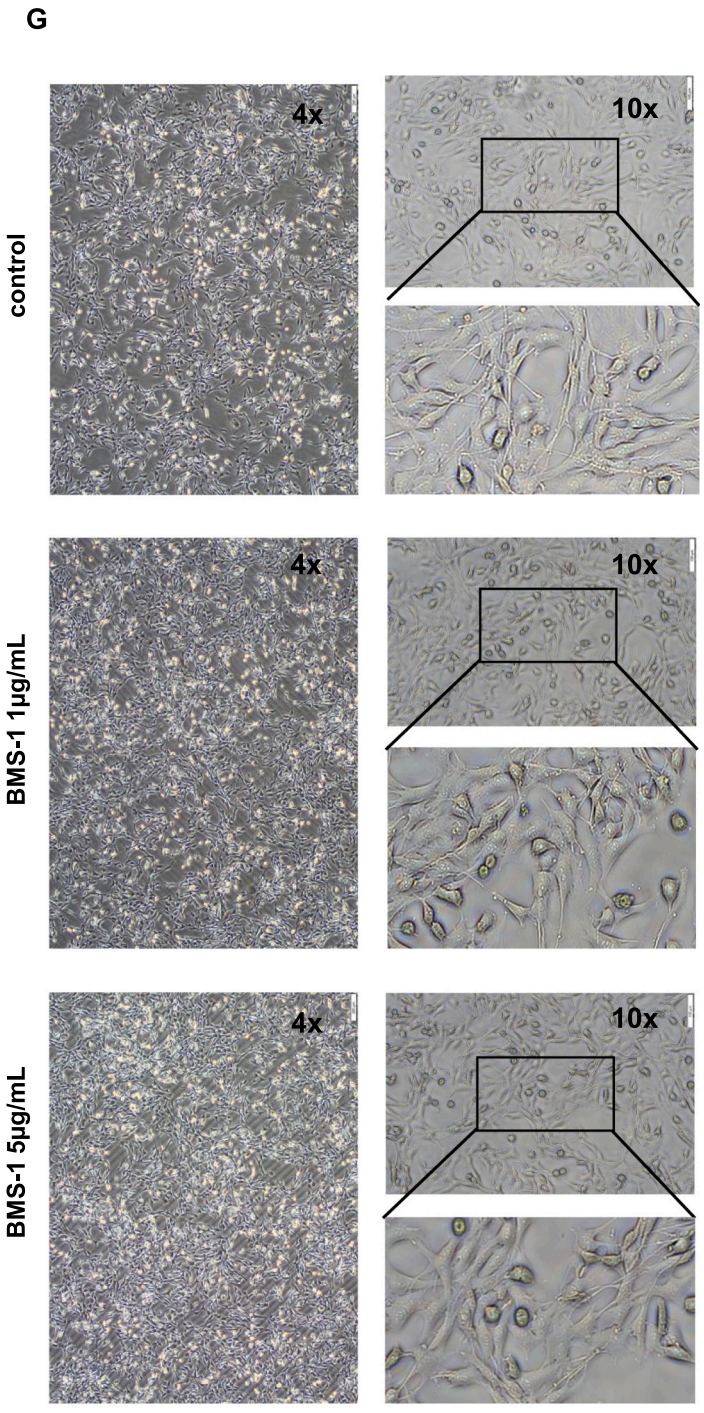

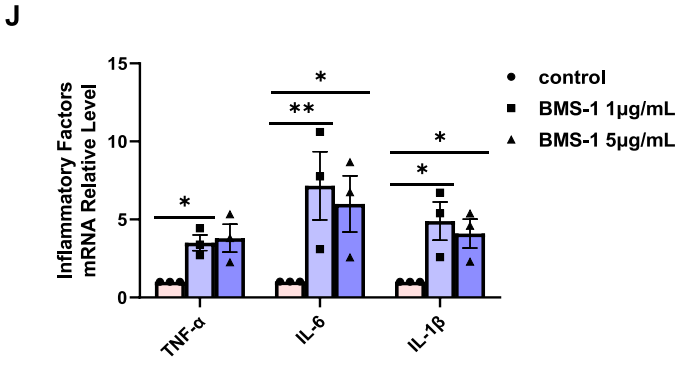

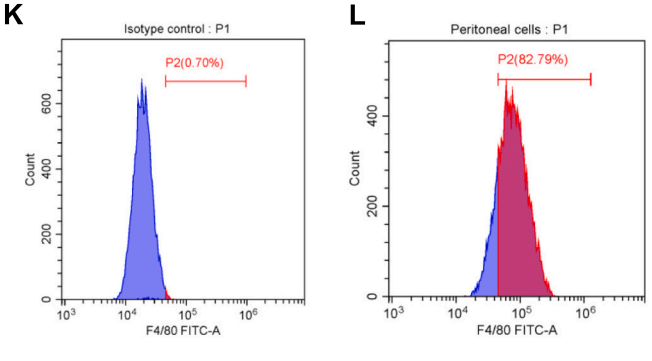

(caption on next page)

Fig. 3. The effect of PD-1/PD-L1 inhibitor BMS-1 on cardiomyocytes and macrophages.
(A–C) qRT-PCR analysis on the expression of *TNF-α, IL-6, IL-1β* in HL-1 cells (N = 3/group). **(D–F)** qRT-PCR analysis on the expression of Nlrp3, Pycard, *IL-18* in HL-1 cells (N = 3/group). **(G)** Morphology of cells treated with different dosage of BMS-1 under the microscope. Scale bar: 100 μm and 200 μm. **(H and I)** Identification of macrophage phagocytic capacity by ink phagocytosis assay. Scale bar: 50 μm and 100 μm. **(J)** qRT-PCR analysis on the expression of *TNF-α, IL-6, IL-1β* in mouse peritoneal macrophages (N = 3/group). **(K and L)** Flow cytometry analysis of the surface expression of F4/80 on peritoneal lavage cells, with the red area indicating positive expression. Data are expressed as the Means ± SEM, statistical significance was determined using unpaired *t*-test. $^{*}p < 0.05$, $^{**}p < 0.01$.

significant increase in TNF-α expression upon stimulation with LPS (Fig. 6B). Moreover, the relative mRNA levels of TNF-α, IL-1β and IL-6 were significantly upregulated following LPS treatment compared to the control (Fig. 6C–E). These findings confirm successful induction of M1 macrophage polarization by LPS. Interestingly, treatment of hBMSC-Exos significantly suppressed LPS-induced M1 polarization markers (TNF-α, IL-1β and IL-6) and meanwhile enhanced M2 polarization markers (TGF-β, Arg-1 and Il-10) (Fig. 6F–H). Immunofluorescence staining further demonstrated decreased TNF-α and increased Arg-1 expressions in the group treated with hBMSC-Exos and LPS compared to the LPS-only group (Fig. 6I–K). The flow cytometry analysis showed that macrophages polarized to the M1 type after LPS treatment, while treatment with both hBMSC-Exos and LPS facilitated their transition from the M1 to the M2 type (Fig. 6L). These results provided evidence that hBMSC-Exos can effectively inhibit M1 polarization and promote M2 polarization of RAW 264.7 macrophages.

3.8. hBMSC-Exos suppressed M2 to M1 polarization of cardiac macrophages in melanoma mice induced by PD-1/PD-L1 inhibitor

To investigate the effect of hBMSC-Exos on macrophage phenotypes treated with PD-1/PD-L1 inhibitor in melanoma mice, we collected heart tissue sections from mice for immunochemical (IHC) staining. The results depicted in Fig. 7A–F showed a significant increase in INOS expression and a significant decrease in CD163 expression in the BMS-1-treated group compared with control, which were reversed by hBMSC-Exos administration. There were no notable changes in the expression of INOS and CD163 between the control and the hBMSC-Exos alone group (Fig. 7A–F). Additionally, the expression levels of M1-type macrophage markers, including TNF-α, IL-6, and IL-1β, were significantly increased following BMS-1 treatment compared to the control group, indicating the promotion of M1-type polarization of macrophages in melanoma mice. However, these changes were effectively reversed by the administration of hBMSC-Exos (Fig. 7E–I). Furthermore, hBMSC-Exos treatment also enhanced the expression of M2-type macrophage markers, such as Arg-1, TGF-β, and IL-10, when compared to the BMS-1-treated group (Fig. 7J–L). These findings suggest that hBMSC-Exos can inhibit PD-1/PD-L1-induced polarization of M1 macrophages and promote M2 macrophage polarization in our melanoma mouse models following BMS-1 treatment.

3.9. hBMSC-Exos attenuated M1 macrophage polarization-induced myocardial pyroptosis

To investigate whether PD-1/PD-L1 inhibitor induced myocardial injury was associated myocardial pyroptosis, we detected pyroptotic markers in the heart tissue of mice by using Western blot analysis. As shown in Fig. 8A-C, BMS-1 significantly increased the expression of inflammasome adaptor protein ASC and the ratio of Cleaved Caspase-1 to Caspase-1, which was recovered by hBMSC-Exos treatment. ASC is a junction protein that contains a caspase activation and recruitment domain (CARD), which binds and promotes the activation of caspase-1, thereby activating the Caspase-1 into the Cleaved Caspase-1, and subsequently inducing pyroptosis. Similarly, the administration of BMS-1 also led to a significant rise in the cardiac NLRP3 protein expression, the ratio of Cleaved-GSDMD to GSDMD, and serum level of IL-18, as well as increased mRNA expression levels of myocardial pyroptosis markers, such as Nlrp3, Pycard, and IL-18, compared to the control group. Interestingly, these effects were effectively attenuated by the treatment with hBMSC-Exos (Fig. 8D–J). To further determine whether M1 macrophage polarization induces myocardial pyroptosis and to explore the potential role of hBMSC-Exos involved in this process, we co-cultured HL-1 cardiomyocytes and RAW264.7 cells with or without LPS and hBMSC-Exos treatment for 24 h (Fig. 8K). Immunofluorescence and qRT-PCR results revealed an upregulation of pyroptosis markers of HL-1 cells induced by M1 macrophage polarization, which was attenuated by hBMSC-Exos treatment (Fig. 8L–P).

3.10. hBMSC-Exos combined with BMS-1 administration minorized the tumor size in melanoma mice

The tumor sizes of mice from various groups were showed in Fig. S3 and Table S5. Treatment with either BMS-1 or hBMSC-Exo alone resulted in a inhibitory trend on tumor growth, although there were large individual differences within the groups and led to no significant difference when compared to the control group. However, a significant inhibition of tumor growth was observed in melanoma mice treated with the combination of BMS-1 and hBMSC-Exos (Fig. S3B–C). Data in Table S5 revealed that BMS-1 restrained tumors in 66.67 % of the animals; hBMSC-Exos suppressed tumors in 50 % of the animals; and the combination of both inhibited tumors in 83.33 % of the animals. These results suggested that hBMSC-Exos do not exacerbate tumors, but rather exhibit an inhibitory effect on tumor growth.

4. Discussion

The main finding of this study is that hBMSC-Exos alleviate myocardial injury induced by PD-1/PD-L1 inhibitor BMS-1, and possess the potential to suppress tumor growth. Our results demonstrate that BMS-1, as a representative ICI, suppresses M2 polarization while enhancing M1 polarization of macrophages, leading to cardiomyocyte pyroptosis and subsequent myocardial injury. Interestingly, hBMSC-Exos effectively counteracted the adverse impact of BMS-1, and demonstrated inhibitory effects on melanoma growth whether administered alone or in combination with BMS-1. This research highlights the association between PD-1/PD-L1 inhibitor-induced myocardial injury and pyroptosis, as well as the crucial role of M1 macrophages in triggering this process. Importantly, our study pioneers the use of hBMSC-Exos in alleviating myocardial injury caused by ICIs. These findings suggest that hBMSC-Exos hold promise for mitigating cardiomyocyte-related side effect associated with ICIs in cancer treatment, thus opening up new possibilities for therapeutic interventions in oncology.

In our current research, we found infiltrated lymphocytes in the cardiac tissue after HE staining, accompanied by a certain degree of cell necrosis, and observed an increase in the transformation of M2 to M1 macrophages in both cardiac tissue and peritoneal macrophages following the administration of BMS-1 to mice. This was evidenced by elevated levels of TNF-α, IL-6, and IL-1β. Our findings are further supported by single-cell transcriptomic analysis in human patients in the absence or present of ICI-associated myocarditis, where we identified three specific markers including CD68, CD14 and CD163 for macrophages and monocytes. As illustrated in Fig. 1B, the M1 macrophage polarization caused by ICIs may be attributed to the decreased oxidative phosphorylation and increased expression of interferon γ (IFN-γ), which was also described in previously studies [51,52]. Numerous prior studies have demonstrated the ability of stem cell-derived exosomes to promote

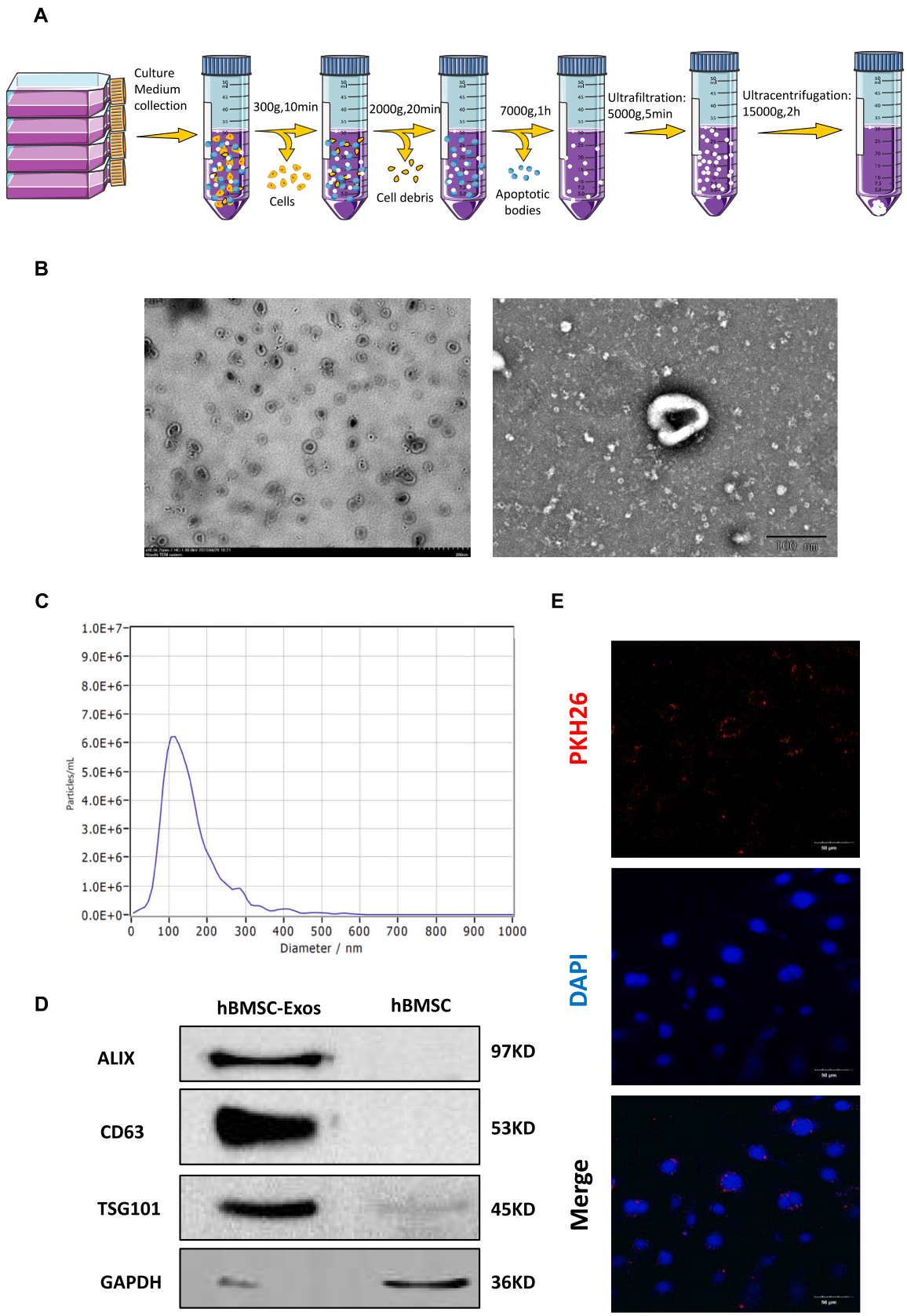

Fig. 4. Extraction and identification of hBMSC-Exos.
(A) Schematic presentation on the extraction of exosomes from bone marrow mesenchymal stem cells by differential and ultra-high-speed centrifugation. **(B)** Exosomes morphology under transmission electron microscope (TEM). Scale bar: 200 nm and 100 nm. **(C)** Size distribution of exosomes (with dilution factor of 2000) detected by NTA. **(D)** Protein levels of ALIX, CD63, TSG101 and GAPDH in hBMSC-Exos and hBMSCs detected by western blot. **(E)** Confocal images showing the uptake of PKH-26-labelled exosomes by macrophage. Exosomes were labelled with PKH-26 (red), and nuclei were labelled with DAPI (blue). Scale bar: 50 μm.

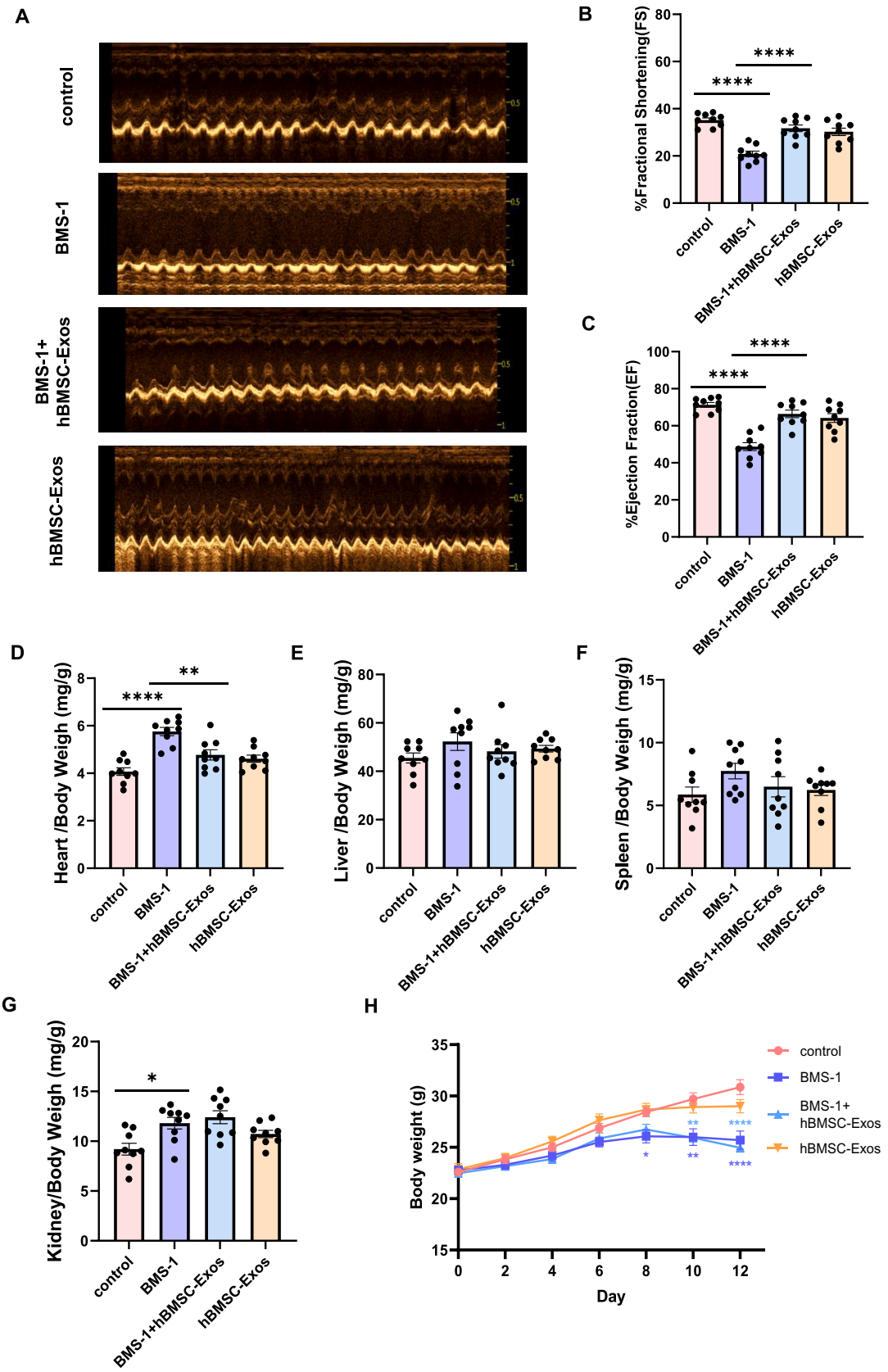

Fig. 5. The effect of hBMSC-Exos on BMS-1-caused cardiac dysfunction, changes in organ and body weight of melanoma mice.
(A) Representative images of echocardiography exhibiting changes in cardiac function in each group. **(B and C)** Echocardiographic analysis of ejection fraction (EF), fractional shortening (FS) (N = 9/group). **(D–G)** Ratio of heart weight, liver weight, kidney weight and spleen weight to the body weight. **(H)** Changes in body weight. Data are present as Mean ± SEM, statistical significance was determined using one-way ANOVA. $^{*}p < 0.05$, $^{**}p < 0.01$, $^{****}p < 0.0001$.

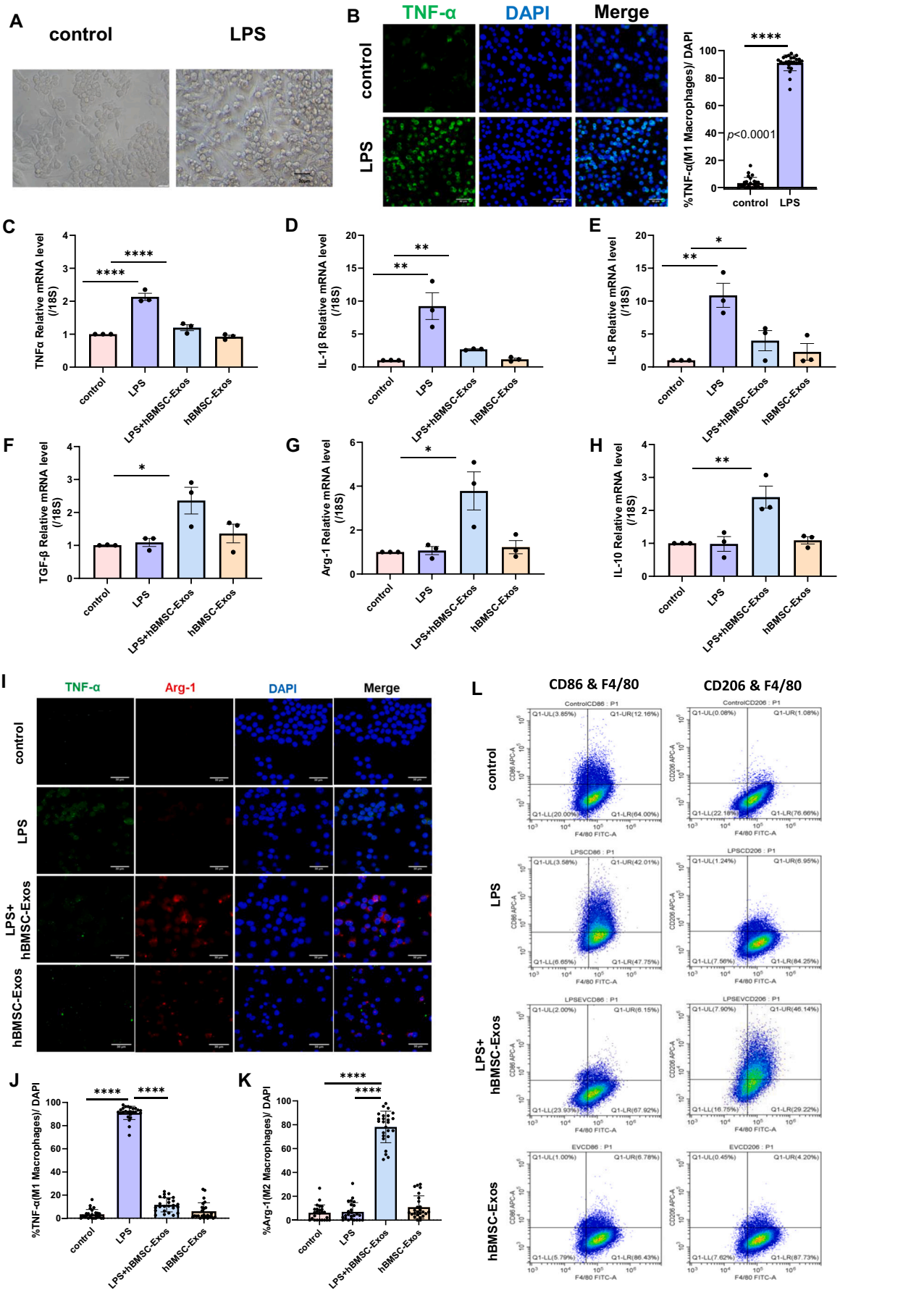

(caption on next page)

Fig. 6. The effect of hBMSC-Exos on the polarization of RAW264.7 cells with or without the treatment of LPS.
(A) Morphology of RAW264.7 with or without the treatment LPS under the microscope. Scale bar: 50 μm. **(B)** Confocal images and quantitative analysis of the expression of TNF-α in RAW264.7 cells with or without the treatment of LPS (N = 25/group). TNF-α were labelled with Dylight 488-conjugated goat anti-rabbit IgG (green), and nuclei were labelled with DAPI (blue). Scale bar: 50 μm. **(C–E)** qRT-PCR analysis on the expressions of *TNF-α, IL-6, IL-1β* in RAW264.7 cells (N = 3/group). **(F–H)**. qRT-PCR analysis on the expressions of *Arg-1, TGF-β, IL-10* in RAW264.7 cells (N = 3/group). **(I)** Confocal images showing the expressions of TNF-α, Arg-1 in RAW264.7 cells under the influence of hBMSC-Exos and LPS (N = 25/group). TNF-α were labelled with Dylight 488-conjugated goat anti-rabbit IgG (green), Arg-1 was labelled with Cy3-conjugated goat anti-rabbit IgG (red), and nuclei were labelled with DAPI (blue). Scale bar: 30 μm. **(J and K)** Quantitative analysis of the expressions of TNF-α in M1 macrophages and Arg-1 in M2 macrophages (N = 25/group). **(L)** Flow cytometry analysis shows that RAW264.7 cells are confidently polarized in different directions in response to LPS and hBMSC-Exos. Data are expressed as the Mean ± SEM, statistical significance was determined using one-way ANOVA. $^{*}p < 0.05$, $^{**}p < 0.01$, $^{****}p < 0.0001$.

the polarization of M2 macrophages while inhibiting the polarization of M1 macrophages [3,12,53], which was aligned with our experimental findings that hBMSC-Exos reversed ICIs-associated macrophage transition. Zhao et al. proposed that miR-182, contained within exosomes, mediates macrophage polarization through the TLR4/NF-κB/PI3K/Akt pathway [3]. Similarly, Ning et al. concluded that exosomes secreted by bone marrow-derived mesenchymal stem cells treated with FNDC5, a transmembrane protein, can promote the polarization of M2 macrophages through the NF-κB signaling pathway and Nrf2/HO-1 axis [53]. Deng et al. discovered that extracellular vesicles can induce M2 transformation in macrophages by activating the S1P/SK1/S1PR pathway, consequently reducing myocardial cell death [12]. Although these pathways, as elucidated in the aforementioned studies, are likely to contribute to the cardiac outcomes observed in our experiments, we discovered that macrophage polarization-induced pyroptosis plays an essential role in BMS-1-induced cardiac anomalies, which may also be the key mechanism that hBMSC-Exos protected against these myocardial adverse effects.

Previous studies have highlighted the significant role of pyroptosis in the pathogenesis and progression of various cardiac diseases, such as myocardial infarction, dilated cardiomyopathy, chronic heart failure, autoimmune myocarditis, and viral myocarditis [54–57]. However, little is known about pyroptosis in ICIs-induced myocardial damage and its targeted treatment strategy. Our study revealed that PD-1/PD-L1 inhibitors cannot directly induce inflammation and pyroptosis in cardiomyocytes. Even when treated with BMS-1, no pyroptosis was observed in HL-1 cardiomyocytes. However, co-culture LPS-induced M1 macrophages with cardiomyocytes significantly triggered cardiac inflammation and pyroptosis. Moreover, elevated ASC, cleaved caspase-1, cleaved-GSDMD/GSDMD and NLRP3 were observed in heart tissue from mice treated with BMS-1. These findings supported that M1 macrophages play a crucial role in inducing cardiac pyroptosis through the classical pyroptosis pathway dependent on caspase-1, which align with the description by Lee et al. who proposed that M1 macrophages upregulate caspase-1, caspase-11, GSDMD, and IL-1β in cardiac fibroblasts, subsequently inducing pyroptosis in cardiac cells [58]. In the present study, the use of ICIs stimulated the polarization of M1 macrophages, leading to the pyroptosis of cardiomyocytes. Consequently, this process resulted in structural changes in the heart and compromised cardiac function. The observed myofibrillar disruption, substantial decrease in EF and FS, reduced posterior wall thickness, increased end systolic LV diameter and volume, as well as increased heart weight in BMS-1-treated mice, indicate myocardial injury, cardiac systolic dysfunction and the presence of dilated cardiomyopathy. The augmentation of the heart weight may be attributed to the development of myocardial edema, pericardial effusions, and increased heart volume caused by PD-1/L1 inhibitor [59,60]. Importantly, our study highlighted that hBMSC-Exos remarkedly mitigated BMS-1-caused myocardial pyroptosis and cardiac dysfunction, which is consistent with the previous findings that MSC-Exos reduced pyroptosis in ischemia reperfusion injury, myocardial infarction and doxorubicin-induced cardiomyopathy [26,61,62]. Nevertheless, the increased kidney weight was failed to alter by hBMSC-Exos. Further investigation is needed to determine the specific reasons behind this observation and the role of hBMSC-Exos in ICIs-related renal side effect [63].

Based on the aforementioned findings, concerns arose regarding the potential of hBMSC-Exos to exacerbate melanoma by influencing M2 macrophage polarization, as indicated in some articles [64]. Surprisingly, our data revealed that hBMSC-Exos, either alone or in conjunction with ICIs, do not promote but inhibit tumor progression. These findings hold promise for the future application of hBMSC-Exos in tumor therapy especially when combined with ICIs. However, further study with larger number of experimental animal samples should be conducted in order to acquire more reliable results. The mechanisms underlying these experimental results are likely to be very complex, as the relationship between hBMSC-Exos and tumors remains controversial. One study suggested that hBMSC-Exos delivering miR-21-5p after hypoxia pre-challenge can promote lung cancer development by facilitating macrophage M2 polarization and reducing apoptosis [65]. Another study indicated that exosomes secreted by tumor- associated MSCs accelerate breast cancer metastasis by driving the polarization of M2 macrophages with stronger immunosuppressive activity [66]. On the contrary, there are also studies showing that hBMSC-Exos can suppress tumor progression. Pakravan et al. demonstrated that hBMSC-Exos reduced the expression of VEGF *via* the mTOR/HIF-1α signaling axis, resulting in the inhibition of tumor growth by restraining angiogenesis [67]. Additionally, evidence has also shown that hBMSC-Exos carrying miR-222-3p negatively regulate the IRF2/INPP4B signaling pathway, thereby inhibiting proliferation and promoting cell apoptosis, ultimately suppressing tumor growth [68]. The effects of exosomes on tumors may involve various factors and aforementioned mechanisms. The ultimate outcome may arise from the antagonistic interplay of these opposing factors. It's noteworthy that the utilized stem cells contaminated with tumor cells or cells that underwent spontaneous transformation may influence the experimental outcome [69]. The implausibility of the tumor-promoting effect shown by the exosomes secreted by these contaminated cells is worth considering. Furthermore, the age of hBMSC donors may lead to different final results [70]. Exosomes secreted by stem cells from younger donors may be less capable of promoting tumor growth, allowing the tumor-inhibiting effect to overshadow the promoting effect. Moreover, the route of hBMSC-Exos administration and the timing of stem cell or exosome exposure to tumors may also be an important factor to consider. When hBMSC-Exos come into contact with tumors in the early stages of tumor development, they may promote angiogenesis in tumor tissue and consequently enhance tumor growth. In our study, hBMSC-Exos were injected after the tumor size reached 50 mm^3, at a stage when the blood vessels in the tumor have already formed, allowing the tumor-suppressive effect of hBMSC-Exos to take precedence.

Taken together, our current evidence indicates that myocyte pyroptosis facilitated by M1 macrophages is one of the mechanisms underlying myocardial injury induced by ICIs. Exosomes has shown promising effectiveness in mitigating ICI-related myocardial damage and inhibiting tumor growth. Additionally, the direct protective impact of hBMSC-Exos on myocardial injury beyond macrophage modulation cannot be overlooked. Further research is warranted to elucidate the therapeutic potential and precise mechanisms of hBMSC-Exos in alleviating myocardial damage induced by ICIs and in suppressing tumors. Utilizing exosomes as a drug delivery system for myocardial therapy is a key focus of our future research to explore the direct effects of stem cell-derived exosomes on myocardial injury.

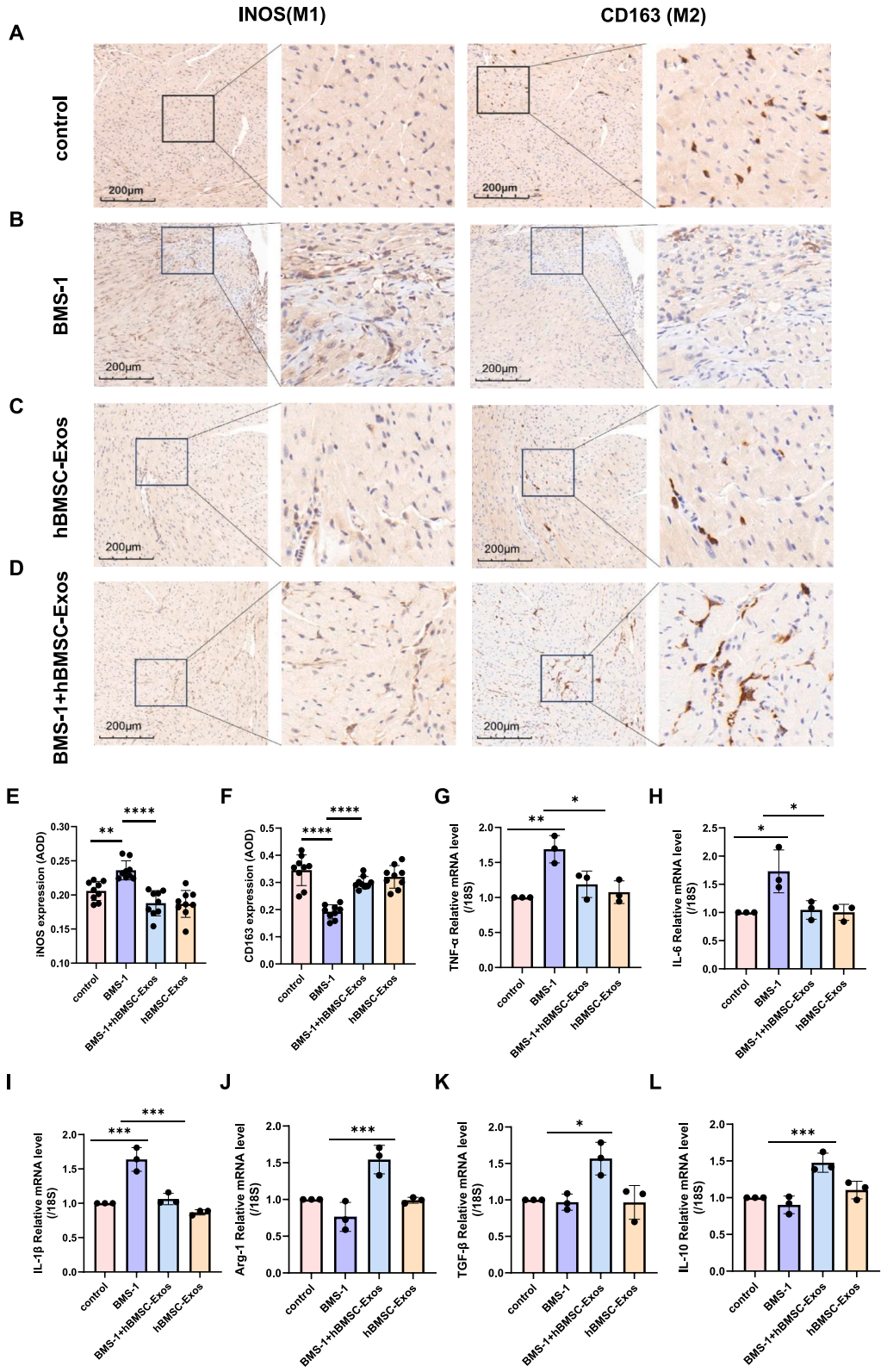

Fig. 7. The effect of hBMSC-Exos and BMS-1 on the polarization of M1 and M2 macrophages in cardiac tissue of melanoma mice.
(A–D) Immunochemical staining images showing the expressions of INOS (M1 macrophage marker) and CD163 (M2 macrophage marker) in cardiac tissue of melanoma mice. Scale bar: 200 μm. **(E and F)** Quantitative analysis of the expressions of INOS and CD163 in immunochemical staining (N = 9/group). **(G–I)** qRT-PCR analysis of the expression of *TNF-α, IL-6, IL-1β* in cardiac tissue (N = 3/group). **(J–L)** qRT-PCR analysis of the expressions of *Arg-1, TGF-β, IL-10* in cardiac tissue (N = 3/group). Data are expressed as the Mean ± SEM, statistical significance was determined using one-way ANOVA. $^{*}p < 0.05$, $^{**}p < 0.01$, $^{***}p < 0.001$, $^{****}p < 0.0001$.

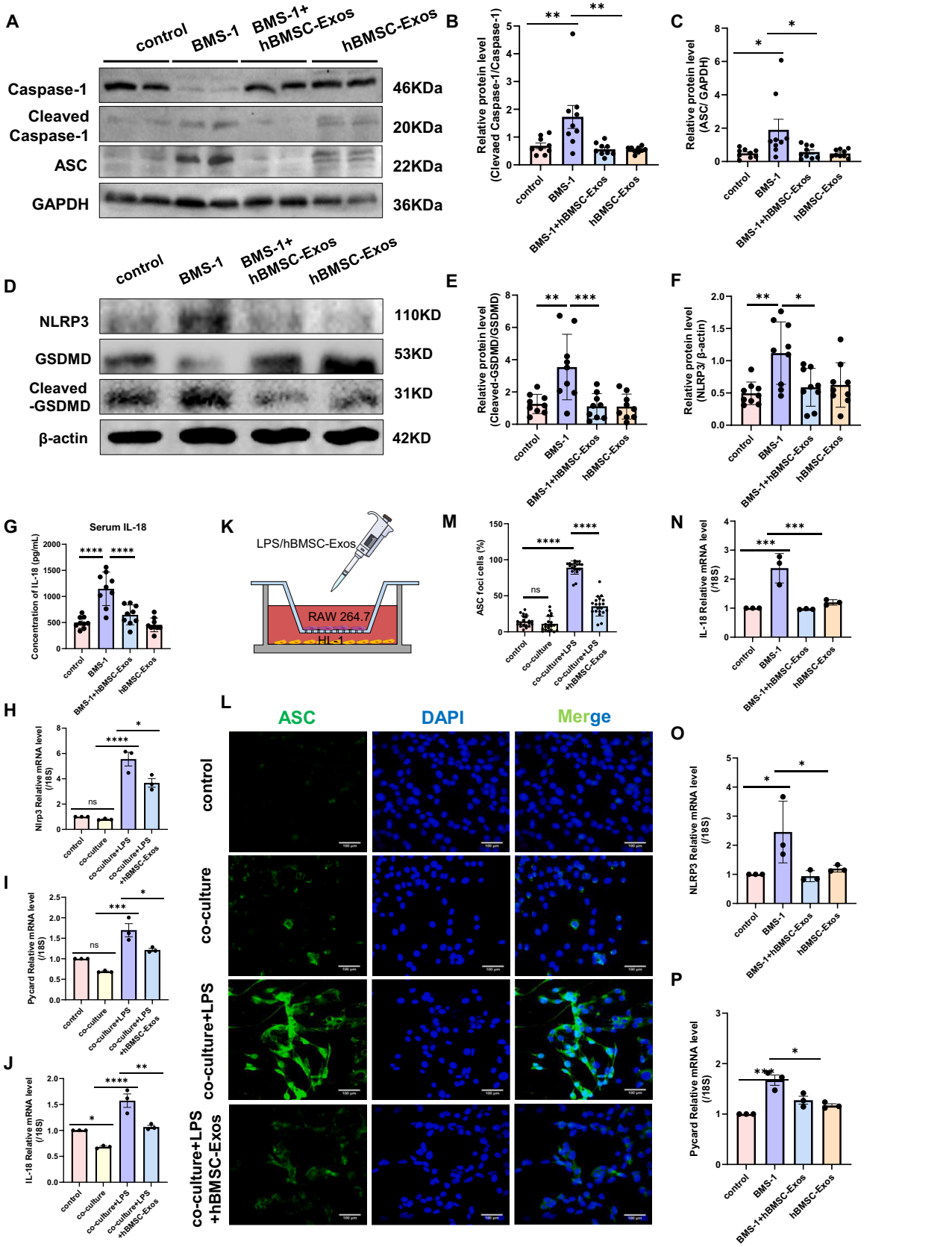

(caption on next page)

Fig. 8. The effect of hBMSC-Exos on inhibiting myocardial pyroptosis.
(A) The representative bands of Caspase-1, Cleaved Caspase-1, ASC in cardiac tissue detected by western blot. **(B and C)** Semi-quantification analysis of the protein levels of Caspase-1, Cleaved Caspase-1, ASC in cardiac tissue (N = 9/group). **(D)** The representative bands of NLRP3, Cleaved- GSDMD, GSDMD, β-actin in cardiac tissue detected by western blot. **(E and F)** Semi-quantification analysis of the protein levels of NLRP3, Cleaved-GSDMD, GSDMD, β-actin in cardiac tissue (N = 9/group). **(G)** Quantitation of IL-18 in the plasma samples of mice measured by ELISA. **(H–J)** qRT-PCR analysis of the expressions of *Nlrp3*, *Pycard*, *IL-18* in HL-1 cardiomyocytes (N = 3/group). **(K)** Schematic presentation on co-culture of RAW264.7 cells and HL-1 cardiomyocytes. **(L)** Confocal images showing the expression of ASC in HL-1 cardiomyocytes co-cultured or not co-cultured with RAW264.7 cells under different conditions of LPS and hBMSC-Exos treatment. ASC were labelled with Dylight 488-conjugated goat anti-rabbit IgG (green), and nuclei were labelled with DAPI (blue). Scale bar: 100 μm. **(M)** Quantitative analysis of ASC positive cardiomyocytes shown in confocal images (N = 20/group). **(N–P)** qRT-PCR analysis of the expressions of *IL-18*, *Nlrp3*, *Pycard* in cardiac tissue (N = 3/group). Data are expressed as the Mean ± SEM, statistical significance was determined using one-way ANOVA. $*p < 0.05$, $**p < 0.01$, $***p < 0.001$, $****p < 0.0001$.

CRediT authorship contribution statement

Bingqian Zhou: Writing – original draft, Project administration, Formal analysis, Data curation, Conceptualization. **Qin Qin:** Writing – review & editing, Writing – original draft, Methodology, Formal analysis, Data curation. **Yue Fang:** Writing – review & editing, Writing – original draft, Methodology, Formal analysis, Data curation. **Xiaoyu Liu:** Formal analysis, Data curation. **Mengyu Zhang:** Methodology. **Shuo Wang:** Data curation. **Li Zhong:** Resources, Project administration. **Rui Guo:** Writing – review & editing, Supervision, Resources, Funding acquisition, Conceptualization.

Declaration of competing interest

The authors declare no competing financial interests.

Data availability statement

The data generated or analyzed during the current study are available from the online supplemental materials or from the corresponding author upon reasonable request.

Acknowledgments

This work was funded by the National Natural Science Foundation of China (#32171181), the Hebei Provincial Natural Science Foundation (#H2023201901), the Beijing-Tianjin-Hebei Basic Research Cooperation Special Project (#J230018), and the Interdisciplinary Research Program of Natural Science of Hebei University (#DXK202105).

Appendix A. Supplementary data

Supplementary data to this article can be found online at https://doi.org/10.1016/j.lfs.2024.123108.

References

[1] A. Naimi, R.N. Mohammed, A. Raji, S. Chupradit, A.V. Yumashev, W. Suksatan, et al., Tumor immunotherapies by immune checkpoint inhibitors (ICIs); the pros and cons, Cell Commun. Signal. 20 (2022) 44.
[2] S.T. Jiang, Y.G. Liu, L. Zhang, X.T. Sang, Y.Y. Xu, X. Lu, Immune-related adverse events: a bibliometric analysis, Front. Immunol. 13 (2022) 1096806.
[3] J.R. Hu, R. Florido, E.J. Lipson, J. Naidoo, R. Ardehali, C.G. Tocchetti, et al., Cardiovascular toxicities associated with immune checkpoint inhibitors, Cardiovasc. Res. 115 (2019) 854–868.
[4] R.P. Patel, R. Parikh, K.S. Gunturu, R.Z. Tariq, S.S. Dani, S. Ganatra, et al., Cardiotoxicity of immune checkpoint inhibitors, Curr. Oncol. Rep. 23 (2021) 79.
[5] A.J. Boyle, D.A. Knight, A.L. Sverdlov, D.T.M. Ngo, J.K. Burgess, D.W. Waters, et al., The role of pathological aging in cardiac and pulmonary fibrosis, Aging Dis. 10 (2019) 419–428.
[6] D.Y. Wang, J.-E. Salem, J.V. Cohen, S. Chandra, C. Menzer, F. Ye, et al., Fatal toxic effects associated with immune checkpoint inhibitors: a systematic review and meta-analysis, JAMA Oncol. 4 (2018) 1721–1728.
[7] W. Liang, X. Chen, S. Zhang, J. Fang, M. Chen, Y. Xu, et al., Mesenchymal stem cells as a double-edged sword in tumor growth: focusing on MSC-derived cytokines, Cell. Mol. Biol. Lett. 26 (2021) 3.
[8] Y. Slama, F. Ah-Pine, M. Khettab, A. Arcambal, M. Begue, F. Dutheil, et al., The dual role of mesenchymal stem cells in cancer pathophysiology: pro-tumorigenic effects versus therapeutic potential, Int. J. Mol. Sci. 24 (2023).
[9] Y.Y. Cheng, Z. Gregorich, R.P. Prajnamitra, D.J. Lundy, T.Y. Ma, Y.H. Huang, et al., Metabolic changes associated with cardiomyocyte dedifferentiation enable adult mammalian cardiac regeneration, Circulation 146 (2022) 1950–1967.
[10] R. Kalluri, V.S. LeBleu, The biology, function, and biomedical applications of exosomes, Science 367 (2020) eaau6977.
[11] D. Allan, A. Tieu, M. Lalu, D. Burger, Mesenchymal stromal cell-derived extracellular vesicles for regenerative therapy and immune modulation: progress and challenges toward clinical application, Stem Cells Transl. Med. 9 (2020) 39–46.
[12] S. Deng, X. Zhou, Z. Ge, Y. Song, H. Wang, X. Liu, et al., Exosomes from adipose-derived mesenchymal stem cells ameliorate cardiac damage after myocardial infarction by activating S1P/SK1/S1PR1 signaling and promoting macrophage M2 polarization, Int. J. Biochem. Cell Biol. 114 (2019) 105564.
[13] X.H. Gong, H. Liu, S.J. Wang, S.W. Liang, G.G. Wang, Exosomes derived from SDF1-overexpressing mesenchymal stem cells inhibit ischemic myocardial cell apoptosis and promote cardiac endothelial microvascular regeneration in mice with myocardial infarction, J. Cell. Physiol. 234 (2019) 13878–13893.
[14] C. Han, J. Zhou, C. Liang, B. Liu, X. Pan, Y. Zhang, et al., Human umbilical cord mesenchymal stem cell derived exosomes encapsulated in functional peptide hydrogels promote cardiac repair, Biomater. Sci. 7 (2019) 2920–2933.
[15] T. Li, J. Gu, O. Yang, J. Wang, Y. Wang, J. Kong, Bone marrow mesenchymal stem cell-derived exosomal miRNA-29c decreases cardiac ischemia/reperfusion injury through inhibition of excessive autophagy via the PTEN/Akt/mTOR signaling pathway, Circ. J. 84 (2020) 1304–1311.
[16] Q. Mao, X.L. Liang, C.L. Zhang, Y.H. Pang, Y.X. Lu, LncRNA KLF3-AS1 in human mesenchymal stem cell-derived exosomes ameliorates pyroptosis of cardiomyocytes and myocardial infarction through miR-138-5p/Sirt1 axis, Stem Cell Res. Ther. 10 (2019) 393.
[17] Z. Ping, T. Fangfang, Z. Yuliang, C. Xinyong, H. Lang, H. Fan, et al., Oxidative stress and pyroptosis in doxorubicin-induced heart failure and atrial fibrillation, Oxidative Med. Cell. Longev. 2023 (2023) 4938287.
[18] P. Liu, Z. Zhang, H. Chen, Q. Chen, Pyroptosis: mechanisms and links with diabetic cardiomyopathy, Ageing Res. Rev. 94 (2024) 102182.
[19] L. Sun, H. Yuan, G. Zhao, IL-37 alleviates Coxsackievirus B3-induced viral myocarditis via inhibiting NLRP3 inflammasome-mediated pyroptosis, Sci. Rep. 12 (2022) 20077.
[20] S.L. Fink, B.T. Cookson, Caspase-1-dependent pore formation during pyroptosis leads to osmotic lysis of infected host macrophages, Cell. Microbiol. 8 (2006) 1812–1825.
[21] S. Sadeghi, F.R. Tehrani, S. Tahmasebi, A. Shafiee, S.M. Hashemi, Exosome engineering in cell therapy and drug delivery, Inflammopharmacology 31 (2023) 145–169.
[22] D.H. Ha, H.K. Kim, J. Lee, H.H. Kwon, G.H. Park, S.H. Yang, et al., Mesenchymal stem/stromal cell-derived exosomes for immunomodulatory therapeutics and skin regeneration, Cells (2020) 9.
[23] J. Abello, T.D.T. Nguyen, R. Marasini, S. Aryal, M.L. Weiss, Biodistribution of gadolinium- and near infrared-labeled human umbilical cord mesenchymal stromal cell-derived exosomes in tumor bearing mice, Theranostics 9 (2019) 2325–2345.
[24] Q. Zeng, Y. Zhou, D. Liang, H. He, X. Liu, R. Zhu, et al., Exosomes secreted from bone marrow mesenchymal stem cells attenuate oxygen-glucose deprivation/reoxygenation-induced pyroptosis in PC12 cells by promoting AMPK-dependent autophagic flux, Front. Cell. Neurosci. 14 (2020) 182.
[25] X. Liu, M. Zhang, H. Liu, R. Zhu, H. He, Y. Zhou, et al., Bone marrow mesenchymal stem cell-derived exosomes attenuate cerebral ischemia-reperfusion injury-induced neuroinflammation and pyroptosis by modulating microglia M1/M2 phenotypes, Exp. Neurol. 341 (2021) 113700.
[26] D.K. Singla, T.A. Johnson, Dargani Z. Tavakoli, Exosome treatment enhances anti-inflammatory M2 macrophages and reduces inflammation-induced pyroptosis in doxorubicin-induced cardiomyopathy, Cells (2019) 8.
[27] Y. Tan, R. Sun, L. Liu, D. Yang, Q. Xiang, L. Li, et al., Tumor suppressor DRD2 facilitates M1 macrophages and restricts NF-kappaB signaling to trigger pyroptosis in breast cancer, Theranostics 11 (2021) 5214–5231.
[28] X. Wei, F. Xie, X. Zhou, Y. Wu, H. Yan, T. Liu, et al., Role of pyroptosis in inflammation and cancer, Cell. Mol. Immunol. 19 (2022) 971–992.
[29] M.A. Ismahil, T. Hamid, S.S. Bansal, B. Patel, J.R. Kingery, S.D. Prabhu, Remodeling of the mononuclear phagocyte network underlies chronic inflammation and disease progression in heart failure: critical importance of the cardiosplenic axis, Circ. Res. 114 (2014) 266–282.
[30] K.R. King, A.D. Aguirre, Y.X. Ye, Y. Sun, J.D. Roh, R.P. Ng Jr., et al., IRF3 and type I interferons fuel a fatal response to myocardial infarction, Nat. Med. 23 (2017) 1481–1487.

[31] G. Bajpai, C. Schneider, N. Wong, A. Bredemeyer, M. Hulsmans, M. Nahrendorf, et al., The human heart contains distinct macrophage subsets with divergent origins and functions, Nat. Med. 24 (2018) 1234–1245.
[32] J. Cai, Q. Qi, X. Qian, J. Han, X. Zhu, Q. Zhang, et al., The role of PD-1/PD-L1 axis and macrophage in the progression and treatment of cancer, J. Cancer Res. Clin. Oncol. 145 (2019) 1377–1385.
[33] Y. Chen, Y. Liu, Y. Wang, X. Chen, C. Wang, X. Chen, et al., Prevotellaceae produces butyrate to alleviate PD-1/PD-L1 inhibitor-related cardiotoxicity via PPARalpha-CYP4X1 axis in colonic macrophages, J. Exp. Clin. Cancer Res. 41 (2022) 1.
[34] Y. Chen, Y. Liu, Y. Wang, X. Chen, C. Wang, X. Chen, et al., Prevotellaceae produces butyrate to alleviate PD-1/PD-L1 inhibitor-related cardiotoxicity via PPARα-CYP4X1 axis in colonic macrophages, J. Cancer Res. Clin. Oncol. 41 (2022) 1.
[35] W. Xia, C. Zou, H. Chen, C. Xie, M. Hou, Immune checkpoint inhibitor induces cardiac injury through polarizing macrophages via modulating microRNA-34a/Kruppel-like factor 4 signaling, Cell Death Dis. 11 (2020) 575.
[36] H. Ning, H. Chen, J. Deng, C. Xiao, M. Xu, L. Shan, et al., Exosomes secreted by FNDC5-BMMSCs protect myocardial infarction by anti-inflammation and macrophage polarization via NF-κB signaling pathway and Nrf2/HO-1 axis, Stem Cell Res. Ther. 12 (2021) 519.
[37] J. Zhao, L. Li, J. Hu, F. Chen, S. Qiao, X. Sun, L. Gao, J. Xie, B. Xu, Mesenchymal stromal cell-derived exosomes attenuate myocardial ischaemia reperfusion injury through miR 182 regulated macrophage polarization, Cardiovasc. Res. 115 (2019) 1205–1216.
[38] R. Xu, F. Zhang, R. Chai, W. Zhou, M. Hu, B. Liu, et al., Exosomes derived from pro-inflammatory bone marrow-derived mesenchymal stem cells reduce inflammation and myocardial injury via mediating macrophage polarization, J. Cell. Mol. Med. 23 (2019) 7617–7631.
[39] H. Zhu, F.X. Galdos, D. Lee, S. Waliany, Y.V. Huang, J. Ryan, et al., Identification of pathogenic immune cell subsets associated with checkpoint inhibitor-induced myocarditis, Circulation 146 (2022) 316–335.
[40] J.E. Salem, M. Bretagne, B. Abbar, S. Leonard-Louis, S. Ederhy, A. Redheuil, et al., Abatacept/ruxolitinib and screening for concomitant respiratory muscle failure to mitigate fatality of immune-checkpoint inhibitor myocarditis, Cancer Discov. 13 (2023) 1100–1115.
[41] J. Chen, Z. Ye, C. Huang, M. Qiu, D. Song, Y. Li, et al., Lipid nanoparticle-mediated lymph node-targeting delivery of mRNA cancer vaccine elicits robust CD8(+) T cell response, Proc. Natl. Acad. Sci. USA 119 (2022) e2207841119.
[42] T.G. Gergely, D. Kucsera, V.E. Tóth, T. Kovács, N.V. Sayour, Z.D. Drobni, et al., Characterization of immune checkpoint inhibitor-induced cardiotoxicity reveals interleukin-17A as a driver of cardiac dysfunction after anti-PD-1 treatment, Br. J. Pharmacol. 180 (6) (2023) 740–761.
[43] R. Guo, J. Ren, Alcohol dehydrogenase accentuates ethanol-induced myocardial dysfunction and mitochondrial damage in mice: role of mitochondrial death pathway, PLoS One 5 (2010) e8757.
[44] A. Iglesias-Linares, J.K. Hartsfield Jr., Cellular and molecular pathways leading to external root resorption, J. Dent. Res. 96 (2017) 145–152.
[45] X. Liu, Y. Liu, X. Chen, C. Wang, X. Chen, W. Liu, et al., Multi-walled carbon nanotubes exacerbate doxorubicin-induced cardiotoxicity by altering gut microbiota and pulmonary and colonic macrophage phenotype in mice, Toxicology 435 (2020) 152410.
[46] K.A. Overmyer, C. Thonusin, N.R. Qi, C.F. Burant, C.R. Evans, Impact of anesthesia and euthanasia on metabolomics of mammalian tissue: studies in a C57BL/6J mouse model, PLoS One 10 (2015) e0117232.
[47] C. Wang, Y.H. Xu, H.Z. Xu, K. Li, Q. Zhang, L. Shi, et al., PD-L1 blockade TAM-dependently potentiates mild photothermal therapy against triple-negative breast cancer, J. Nanobiotechnol. 21 (2023) 476.
[48] I.D. Odell, D. Cook, Immunofluorescence techniques, J. Invest. Dermatol. 133 (2013) 1–4.
[49] M.L. Axelrod, W.C. Meijers, E.M. Screever, J. Qin, M.G. Carroll, X. Sun, et al., T cells specific for alpha-myosin drive immunotherapy-related myocarditis, Nature 611 (2022) 818–826.
[50] W. Liu, M. Yu, D. Xie, L. Wang, C. Ye, Q. Zhu, et al., Melatonin-stimulated MSC-derived exosomes improve diabetic wound healing through regulating macrophage M1 and M2 polarization by targeting the PTEN/AKT pathway, Stem Cell Res. Ther. 11 (2020) 259.
[51] H. Xiong, S. Mittman, R. Rodriguez, M. Moskalenko, P. Pacheco-Sanchez, Y. Yang, et al., Anti-PD-L1 treatment results in functional remodeling of the macrophage compartment, Cancer Res. 79 (2019) 1493–1506.
[52] S.K. Wculek, I. Heras-Murillo, A. Mastrangelo, D. Mananes, M. Galan, V. Miguel, et al., Oxidative phosphorylation selectively orchestrates tissue macrophage homeostasis, Immunity 56 (2023), 516-30 e9.
[53] H. Ning, H. Chen, J. Deng, C. Xiao, M. Xu, L. Shan, et al., Exosomes secreted by FNDC5-BMMSCs protect myocardial infarction by anti-inflammation and macrophage polarization via NF-kappaB signaling pathway and Nrf2/HO-1 axis, Stem Cell Res. Ther. 12 (2021) 519.
[54] Z. Zhaolin, L. Guohua, W. Shiyuan, W. Zuo, Role of pyroptosis in cardiovascular disease, Cell Prolif. 52 (2019) e12563.
[55] N. An, Y. Gao, Z. Si, H. Zhang, L. Wang, C. Tian, et al., Regulatory mechanisms of the NLRP3 inflammasome, a novel immune-inflammatory marker in cardiovascular diseases, Front. Immunol. 10 (2019) 1592.
[56] N. Liu, H. Su, Y. Zhang, Z. Liu, J. Kong, Cholecalciterol cholesterol emulsion attenuates experimental autoimmune myocarditis in mice via inhibition of the pyroptosis signaling pathway, Biochem. Biophys. Res. Commun. 493 (2017) 422–428.
[57] Y. Wang, L. Jia, J. Shen, Y. Wang, Z. Fu, S.A. Su, et al., Cathepsin B aggravates coxsackievirus B3-induced myocarditis through activating the inflammasome and promoting pyroptosis, PLoS Pathog. 14 (2018) e1006872.
[58] C.Y. Lee, S. Lee, S. Jeong, J. Lee, H.H. Seo, S. Shin, et al., Suppressing pyroptosis augments post-transplant survival of stem cells and cardiac function following ischemic injury, Int. J. Mol. Sci. 22 (2021).
[59] S.H. Zhao, H. Yun, C.Z. Chen, Y.Y. Chen, J.Y. Lin, M.S. Zeng, et al., Applying quantitative CMR parameters for detecting myocardial lesion in immune checkpoint inhibitors-associated myocarditis, Eur. J. Radiol. 156 (2022) 110558.
[60] F. Pirozzi, R. Poto, L. Aran, A. Cuomo, M.R. Galdiero, G. Spadaro, et al., Cardiovascular toxicity of immune checkpoint inhibitors: clinical risk factors, Curr. Oncol. Rep. 23 (2021) 13.
[61] Z. Hu, Y. Yuan, X. Zhang, Y. Lu, N. Dong, X. Jiang, et al., Human umbilical cord mesenchymal stem cell-derived exosomes attenuate oxygen-glucose deprivation/reperfusion-induced microglial pyroptosis by promoting FOXO3a-dependent mitophagy, Oxidative Med. Cell. Longev. 2021 (2021) 6219715.
[62] Y. Liu, P. Li, C. Qiao, T. Wu, X. Sun, M. Wen, et al., Chitosan hydrogel enhances the therapeutic efficacy of bone marrow-derived mesenchymal stem cells for myocardial infarction by alleviating vascular endothelial cell pyroptosis, J. Cardiovasc. Pharmacol. 75 (2020) 75–83.
[63] M.A. Perazella, A.C. Shirali, Immune checkpoint inhibitor nephrotoxicity: what do we know and what should we do? Kidney Int. 97 (2020) 62–74.
[64] A.J. Boutilier, S.F. Elsawa, Macrophage polarization states in the tumor microenvironment, Int. J. Mol. Sci. 22 (2021).
[65] W. Ren, J. Hou, C. Yang, H. Wang, S. Wu, Y. Wu, et al., Extracellular vesicles secreted by hypoxia pre-challenged mesenchymal stem cells promote non-small cell lung cancer cell growth and mobility as well as macrophage M2 polarization via miR-21-5p delivery, J. Exp. Clin. Cancer Res. 38 (2019) 62.
[66] S. Biswas, G. Mandal, S. Roy Chowdhury, S. Purohit, K.K. Payne, C. Anadon, et al., Exosomes produced by mesenchymal stem cells drive differentiation of myeloid cells into immunosuppressive M2-polarized macrophages in breast cancer, J. Immunol. 203 (2019) 3447–3460.
[67] K. Pakravan, S. Babashah, M. Sadeghizadeh, S.J. Mowla, M. Mossahebi-Mohammadi, F. Ataei, et al., MicroRNA-100 shuttled by mesenchymal stem cell-derived exosomes suppresses in vitro angiogenesis through modulating the mTOR/HIF-1alpha/VEGF signaling axis in breast cancer cells, Cell. Oncol. (Dordr) 40 (2017) 457–470.
[68] F. Zhang, Y. Lu, M. Wang, J. Zhu, J. Li, P. Zhang, et al., Exosomes derived from human bone marrow mesenchymal stem cells transfer miR-222-3p to suppress acute myeloid leukemia cell proliferation by targeting IRF2/INPP4B, Mol. Cell. Probes 51 (2020) 101513.
[69] A. Torsvik, G.V. Rosland, A. Svendsen, A. Molven, H. Immervoll, E. McCormack, et al., Spontaneous malignant transformation of human mesenchymal stem cells reflects cross-contamination: putting the research field on track - letter, Cancer Res. 70 (2010) 6393–6396.
[70] W. Zhu, W. Xu, R. Jiang, H. Qian, M. Chen, J. Hu, et al., Mesenchymal stem cells derived from bone marrow favor tumor cell growth in vivo, Exp. Mol. Pathol. 80 (2006) 267–274.